

AD-A264 156



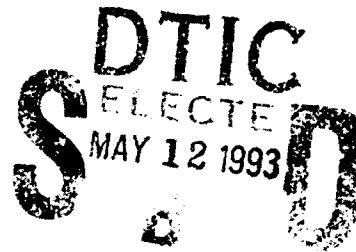
PL-TR-93-2050

2

**AN INVESTIGATION OF METHODS FOR
IMPROVING MODELS OF IONOSPHERIC
PLASMA-DENSITY IRREGULARITIES AND
RADIO-FREQUENCY SCINTILLATION**

James A. Secan
Robert M. Bussey
Edward J. Fremouw
Lee A. Reinleitner

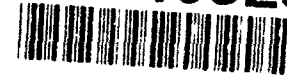
Northwest Research Associates, Inc.
P.O. Box 3027
Bellevue, WA 98009



1 March 1993

Scientific Report No. 1

93-10525



approved for public release; distribution unlimited



**PHILLIPS LABORATORY
Directorate of Geophysics
AIR FORCE MATERIEL COMMAND
HANSCOM AIR FORCE BASE, MA 01731-3010**

93 5 11 19 2

"This technical report has been reviewed and is approved for publication"



SANTIMAY BASU
Contract Manager



JOHN E. RASMUSSEN
Branch Chief



WILLIAM K. VICKERY
Division Director

This document has been reviewed by the ESD Public Affairs Office (PA) and is releasable to the National Technical Information Service (NTIS).

Qualified requestors may obtain additional copies from the Defense Technical Information Center. All others should apply to the National Technical Information Service.

If your address has changed, or if you wish to be removed from the mailing list, or if the addressee is no longer employed by your organization, please notify PL/TSI, Hanscom AFB, MA 01731-5000. This will assist us in maintaining a current mailing list.

Do not return copies of this report unless contractual obligations or notices on a specific document requires that it be returned.

REPORT DOCUMENTATION PAGE			Form Approved OMB No 0704-0188	
Public reporting burden for this collection of information is estimated to average 1 hour per response, including the time for reviewing instructions, searching existing data sources, gathering and maintaining the data needed, and completing and reviewing the collection of information. Send comments regarding this burden estimate or any other aspect of this collection of information, including suggestions for reducing this burden, to Washington Headquarters Services, Directorate for Information Operations and Reports, 1215 Jefferson Davis Highway, Suite 1204, Arlington, VA 22202-4302, and to the Office of Management and Budget, Paperwork Reduction Project (0704-0188), Washington, DC 20503.				
1. AGENCY USE ONLY (Leave blank)	2. REPORT DATE 1 March 1993	3. REPORT TYPE AND DATES COVERED Scientific No. 1		
4. TITLE AND SUBTITLE An Investigation of Methods for Improving Models of Ionospheric Plasma-Density Irregularities and Radio-Frequency Scintillation		5. FUNDING NUMBERS F19628-91-C-0152 PE63707F PR AWS9 TA 10 WU AA		
6. AUTHOR(S) James A. Secan, Robert M. Bussey, Edward J. Fremouw, Lee A. Reinleitner				
7. PERFORMING ORGANIZATION NAME(S) AND ADDRESS(ES) Northwest Research Associates, Inc. P.O. Box 3027 Bellevue, WA 98009		8. PERFORMING ORGANIZATION REPORT NUMBER NWRA-CR-93-R093		
9. SPONSORING/MONITORING AGENCY NAME(S) AND ADDRESS(ES) Phillips Laboratory 29 Randolph Road Hanscom AFB, MA 01731-3010 Contract Manager: Santimay Basu/GPIS		10. SPONSORING/MONITORING AGENCY REPORT NUMBER PL-TR-93-2050		
11. SUPPLEMENTARY NOTES				
12a. DISTRIBUTION/AVAILABILITY STATEMENT approved for public release; distribution unlimited			12b. DISTRIBUTION CODE	
13. ABSTRACT (Maximum 200 words) Many modern military systems used for communications, command and control, navigation, and surveillance depend on reliable and relatively noise-free transmission of radiowave signals through the earth's ionosphere. Small-scale irregularities in the ionospheric density can cause severe distortion, known as radiowave scintillation, of both the amplitude and phase of these signals. The WBMOD computer program can be used to estimate these effects on a wide range of systems. The objective of this study is to investigate improvements to the WBMOD model based on extensive data sets covering both the equatorial and high-latitude regimes. This report summarizes the work completed during the first year, which includes construction of the modeling database, development of a new format for the internal representation of the irregularity strength, and development of new models for the diurnal, latitudinal, seasonal, and longitudinal variations in the equatorial region.				
14. SUBJECT TERMS ionosphere, ionospheric scintillation, radiowave scintillation			15. NUMBER OF PAGES 60	
			16. PRICE CODE	
17. SECURITY CLASSIFICATION OF REPORT Unclassified	18. SECURITY CLASSIFICATION OF THIS PAGE Unclassified	19. SECURITY CLASSIFICATION OF ABSTRACT Unclassified	20. LIMITATION OF ABSTRACT SAR	

CONTENTS

Page

Figures and Tables	iv
Preface	ix
1. Introduction	1
2. Scintillation Database Development	1
2.1 Converting $SI(dB)$ to S_4	1
2.2 Database Design	4
3. Irregularity Models Development	7
3.1 Model for $\log(C_k L)$ PDF	7
3.2 Modeling Philosophy	10
3.3 Latitudinal Variation	11
3.4 Diurnal Variation	15
3.5 Longitudinal Variation	24
3.6 Seasonal Variation	25
3.7 Results of Diurnal/Seasonal/Longitudinal Modeling	25
3.8 Geomagnetic Activity Effects	37
3.8.1 Literature Review	37
3.8.2 Model Development	42
4. Propagation Model Development	46
5. Conclusion	47
References	47

Accession For	
NTIS GRA&I	<input checked="" type="checkbox"/>
DTIC TAB	<input type="checkbox"/>
Unannounced	<input type="checkbox"/>
Justification	
By	
Distribution	
Availability Codes	
DISTRIBUTION STATEMENT	
A-1	

Figures and Tables

Table 1	Data used in the equatorial model development.	1
Figure 1	S_4 distributions from the Kwajalein and Ancon Wideband VHF data sets (top and bottom plots) and derived from the Ascension Island Marisat L-band $SI(dB)$ data set.	3
Table 2	Location of peaks in S_4 distribution plots.	4
Figure 2	Comparison of algorithms for converting $SI(dB)$ to S_4	5
Figure 3	Database structure for data from Ascension Island, Huancayo, and Manila.	6
Figure 4	Distribution of $\log(C_k L)$ during the post-sunset period at Kwajalein and Ancon from the Wideband experiment (VHF).	8
Figure 5	Probability distribution function (PDF) (top plot) and cumulative distribution function (CDF) (bottom plot) for an equatorial station. These were generated using the new three-component PDF model (see text) with the parameters indicated in the side box.	9
Figure 6	Contour plots of the percent of time that S_4 exceeds 0.5 (upper plot) and 0.8 (lower plot) as a function of GMT and day of the year from the Manila-FLEETSAT UHF database. The horizontal dashed lines indicate the equinoxes, the heavy solid and dashed lines indicate the time of E-region sunset (both E-region ends of the field line are in sunset) and F2-region sunset (solar declination, χ , is 107°).	12
Figure 7	Samples of the new equatorial $C_k L$ model formulation. The model parameters used in each are defined in the adjacent boxes. See the text for a description of the model and model parameters.	14
Figure 8	Diurnal behavior of intensity scintillation from the Ascension Island Marisat (VHF) data set. Contours of the percent of the time that SI exceeded 10 dB are plotted as a function of GMT and the day of the year. The heavy solid line shows the variation of $ERSS = 0$ with the day of the year, and the heavy dashed line shows the variation of $\chi = 107^\circ$	16
Figure 9	Diurnal behavior of intensity scintillation from the Ascension Island Marisat (L-band) data set. Contours of the percent of the time that SI exceeded 10 dB are plotted as a function of GMT and the day of the year. The heavy solid line shows the variation of $ERSS = 0$ with the day of the year, and the heavy dashed line shows the variation of $\chi = 107^\circ$	17

Figure 10	Diurnal behavior of intensity scintillation from the Huancayo Marisat (VHF) data set. Contours of the percent of the time that SI exceeded 10 dB are plotted as a function of GMT and the day of the year. The heavy solid line shows the variation of $ERSS = 0$ with the day of the year, and the heavy dashed line shows the variation of $\chi = 107^\circ$.	18
Figure 11	Diurnal behavior of intensity scintillation from the Huancayo Marisat (VHF) data set. Contours of the percent of the time that SI exceeded 10 dB are plotted as a function of GMT and the day of the year. The heavy solid line shows the variation of $ERSS = 0$ with the day of the year, and the heavy dashed line shows the variation of $\chi = 107^\circ$.	19
Figure 12	Diurnal behavior of intensity scintillation from the Huancayo Marisat (VHF) data set. Contours of the percent of the time that SI exceeded 10 dB are plotted as a function of GMT and the day of the year. The heavy solid line shows the variation of $ERSS = 0$ with the day of the year, and the heavy dashed line shows the variation of $\chi = 107^\circ$.	20
Figure 13	(a) Contours of the percent of observations with $S_4 > 0.5$ as a function of GMT and day of the year from the Ascension Island (L-band) data set, $K_p \leq 20$. (b) Same as in (a) for $S_4 > 0.8$. Heavy solid curve is the time of E-region sunset, heavy dashed curve is the time of F-region sunset ($\chi = 107^\circ$), and the two dashed horizontal lines indicate the two equinoxes.	26
Figure 14	(a) Model results for Ascension Island (L-band) corresponding to the data shown in 13(a). (b) Model results for Ascension Island (L-band) corresponding to the data shown in 13(b).	27
Figure 15	(a) Contours of the percent of observations with $S_4 > 0.5$ as a function of GMT and day of the year from the Ascension Island (VHF) data set, $K_p \leq 20$. (b) Same as in (a) for $S_4 > 0.8$. Heavy solid curve is the time of E-region sunset, heavy dashed curve is the time of F-region sunset ($\chi = 107^\circ$), and the two dashed horizontal lines indicate the two equinoxes.	28
Figure 16	(a) Model results for Ascension Island (VHF) corresponding to the data shown in 15(a). (b) Model results for Ascension Island (VHF) corresponding to the data shown in 15(b).	29

Figure 17	(a) Contours of the percent of observations with $S_4 > 0.5$ as a function of GMT and day of the year from the Huancayo (VHF) data set, $K_p \leq 20$. (b) Same as in (a) for $S_4 > 0.8$. Heavy solid curve is the time of E-region sunset, heavy dashed curve is the time of F-region sunset ($\chi = 107^\circ$), and the two dashed horizontal lines indicate the two equinoxes.	30
Figure 18	(a) Model results for Huancayo (VHF) corresponding to the data shown in 17(a). (b) Model results for Huancayo (VHF) corresponding to the data shown in 17(b).	31
Figure 19	(a) Contours of the percent of observations with $S_4 > 0.5$ as a function of GMT and day of the year from the Huancayo (L-band) data set, $K_p \leq 20$. (b) Same as in (a) for $S_4 > 0.8$. Heavy solid curve is the time of E-region sunset, heavy dashed curve is the time of F-region sunset ($\chi = 107^\circ$), and the two dashed horizontal lines indicate the two equinoxes.	32
Figure 20	(a) Model results for Huancayo (L-band) corresponding to the data shown in 19(a). (b) Model results for Huancayo (L-band) corresponding to the data shown in 19(b).	33
Figure 21	(a) Contours of the percent of observations with $S_4 > 0.5$ as a function of GMT and day of the year from the Manila (VHF) data set, $K_p \leq 20$. (b) Same as in (a) for $S_4 > 0.8$. Heavy solid curve is the time of E-region sunset, heavy dashed curve is the time of F-region sunset ($\chi = 107^\circ$), and the two dashed horizontal lines indicate the two equinoxes.	34
Figure 22	(a) Model results for Manila (VHF) corresponding to the data shown in 21(a). (b) Model results for Manila (VHF) corresponding to the data shown in 21(b).	35
Figure 23	Model results for Kwajalein (near-overhead case). Layout and labeling are as in similar plots in Figures 13-22. The two vertical dotted lines indicate the GMT range covered by the Kwajalein-WIDEBAND (VHF) data set.	36
Figure 24	Cumulative distribution of S_4 as a function of day of the year (a) from the Kwajalein-WIDEBAND (VHF) data set, (b) from the Manila-FLEETSAT (VHF) data set (limited to the t_e period covered by the Kwajalein data set). The vertical dotted lines indicate the equinoxes.	38

Figure 25	Occurrence statistics of $S_4 > 0.5$ from the Huancayo VHF data set as a function of TPSS (t_e) and day of the year for three levels of geomagnetic activity as measured by D_{st} : (a) $D_{st} > 0$, (b) $0 \geq D_{st} \geq -50$, and (c) $D_{st} < -50$.	43
Figure 26	Occurrence statistics of $S_4 > 0.5$ from the Huancayo VHF data set as a function of TPSS (t_e) and day of the year for three levels of geomagnetic activity as measured by K_p : (a) $K_p \leq 20$, (b) $20 < K_p \leq 40$, and (c) $K_p > 40$.	44
Figure 27	Occurrence statistics of $S_4 > 0.5$ from the Huancayo VHF data set as a function of TPSS (t_e) and day of the year for three levels of geomagnetic activity as measured by K_p at $t_e = 0$: (a) $K_p \leq 20$, (b) $20 < K_p \leq 40$, and (c) $K_p > 40$.	45

PREFACE

This report summarizes the work completed during the first year of a project focused on improving the WBMOD model of ionospheric scintillation. This work is part of a larger effort which has the overall objective of providing the USAF Air Weather Service with an improved capability for providing support to their customers who are impacted by ionospheric scintillation effects.

We would like to thank Dr. Santimay Basu of the USAF Phillips Laboratory (PL/GPIA) for providing the scintillation data sets from Ascension Island, Huancayo, and Manila, and for his guidance and suggestions for improving the model.

1. Introduction

Many modern military systems used for communications, command and control, navigation, and surveillance depend on reliable and relatively noise free transmission of radiowave signals through the earth's ionosphere. Small-scale irregularities in the ionospheric density can cause severe distortion, known as radiowave scintillation, of both the amplitude and phase of these signals. A basic tool used in estimating these effects on systems is a computer program, WBMOD, based on a single-scatter phase-screen propagation model and a number of empirical models of the global morphology of ionospheric density irregularities. A recent validation of the WBMOD model showed that it was deficient in a number of areas. Much of this deficiency could be traced to the limited coverage of the data used in developing the model (a single station at high latitudes and two stations at equatorial latitudes). The objective of this study is to investigate and implement improvements to the WBMOD model based on more extensive data sets in both the equatorial and high- latitude regimes.

2. Scintillation Database Development

The data to be used in the modeling effort come from two sources. The first is data collected from the Wideband satellite in the 1970s at Ancon, Peru, and Kwajalein Atoll. The second is data collected from the Marisat satellite from Ascension Island and Huancayo, Peru, and from the Fleetsat satellite from Manila, Philippines. The second data set was provided by PL/GPIA. Both data sets were used in a validation of the WBMOD scintillation model, reported in *Secan* [1991]. Table 1 lists the coverage of these data sets. The column headed "IPP" is the geomagnetic (apex) latitude of the 350-km ionospheric penetration point (IPP). For Ancon and Kwajalein, this is defined for the overhead case.

Station	Satellite	IPP	Dates	Points
Ancon	Wideband	0.9	1976-1979	28,550
Huancayo	Marisat	1.6	1976-1984	332,800
Kwajalein	Wideband	4.1	1976-1979	30,420
Manila	Fleetsat	5.8	1981-1985	150,550
Ascension Island	Marisat	-16.5	1980-1989	121,470

Table 1: Data used in the equatorial model development.

2.1 Converting $SI(dB)$ to S_4 . The first step in preparing the $SI(dB)$ data provided by PL for use in modeling was to convert it to the equivalent S_4 value. This was to be done using an algorithm described in *Secan* [1991] (taken from *Whitney* [1974]) based on an empirically derived relationship between the $SI(dB)$ index and the Nakagami m -parameter (Figure 6 in

Whitney [1974]). It is not clear over what range of m values this relationship is valid, in particular if it is valid for low values of m (which translates into high values of S_4). This algorithm uses the following equation to calculate S_4 from $SI(dB)$:

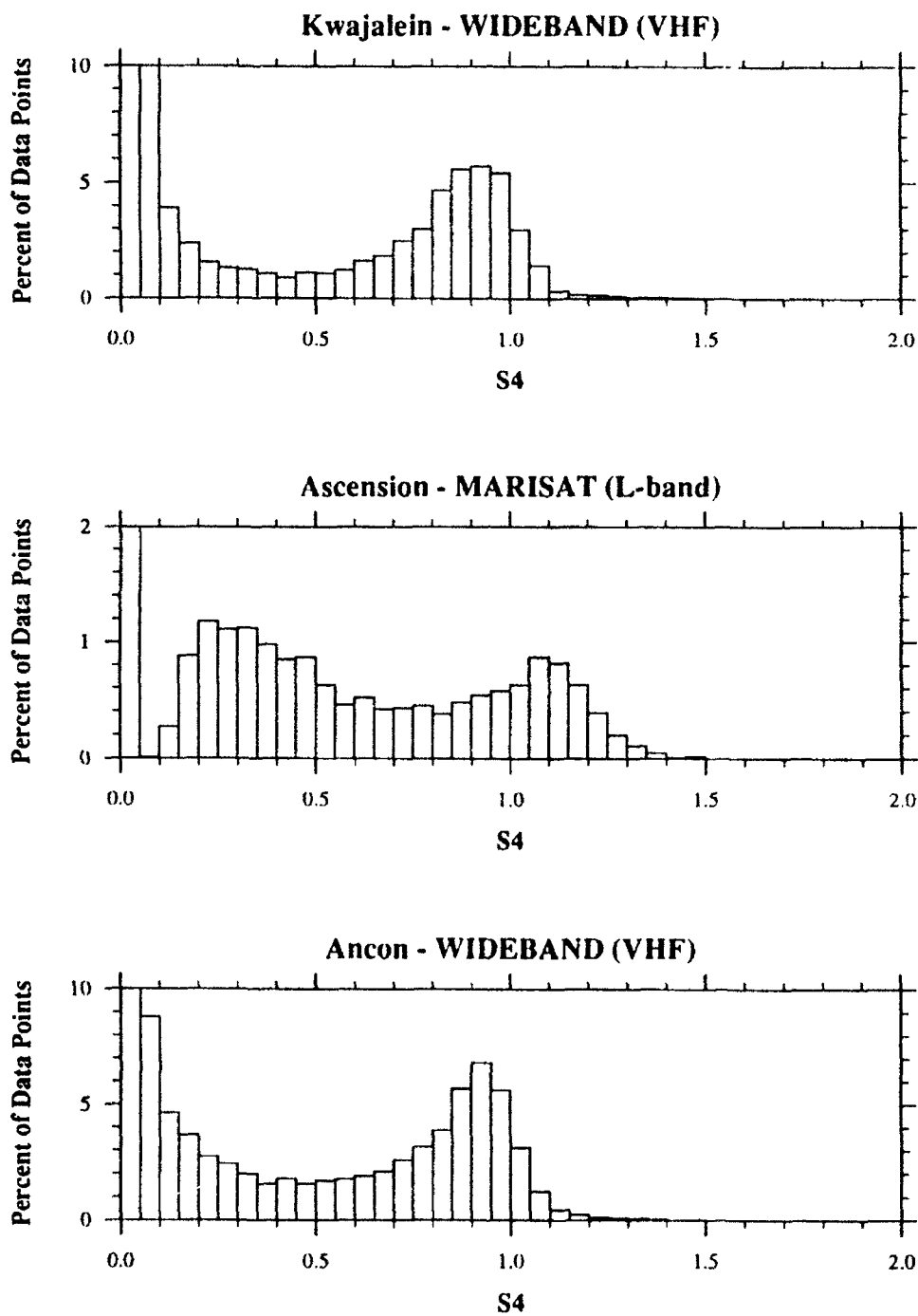
$$S_4 = 0.0735SI(dB)^{0.757} \quad (1)$$

Our concern over the validity of this algorithm was first raised in an analysis of data from Ascension Island which was used in the WBMOD validation study (Secan [1991]). The result of this analysis was that it appeared that the S_4 values derived from the Ascension Island $SI(dB)$ values were roughly 20% too high (see the Appendix in Secan [1991]). A solution to this problem was approached from two directions. First, empirical factors were derived which, when multiplied times the S_4 values generated from the $SI(dB)$ data, led to distributions of S_4 at the PL stations which were in agreement with the distributions seen in the Wideband data sets. Second, a set of digital data from Ascension Island was analyzed by PL/GPIA to calculate both S_4 and $SI(dB)$ to be used to test the empirical relationship generated from the information in Whitney [1974].

The three histogram plots in Figure 1 illustrate the problem. These plots show the distribution of S_4 from the Kwajalein and Ancon Wideband data sets (top and bottoms plots, respectively) and the distribution of S_4 calculated from $SI(dB)$ from the Ascension Island MARISAT L-band data set (middle plot). The data used in generating these distributions spanned the time period from one hour prior to local sunset to eight hours after sunset. Note that the distributions for the two Wideband sets peak just below an S_4 value of 1.0 (at 0.93 for both sets) caused by saturation in the level of intensity scintillation due to Fresnel filtering. The similar peak in the Ascension Island data is at a value of 1.10. While it is possible for S_4 to exceed 1.0 in cases of strong multiple scatter, it is unlikely that the peak in the distribution, which is caused by the saturation effect, would occur above 1.0. Table 2 summarizes the locations of the peaks in the various S_4 data sets. Note that the two Huancayo data sets peak at values above the peaks in the Wideband data sets, and that the Manila data set peaks below the Wideband value.

It is interesting to note that if we regard the S_4 value of 0.93 from both directly-computed Wideband VHF data sets as the expected S_4 value at this peak, a "corrective" multiplier of 0.95 ($\pm 8\%$) for Huancayo VHF data and 1.09 ($\pm 6\%$) for Manila VHF data is needed. Although the data were insufficient for a true S_4 peak in the Wideband L-band data, if we used the Wideband VHF peak of 0.93 also, a corrective multiplier of 0.97 is needed for the Huancayo L-band data. All of these adjustments are quite small, and are essentially indistinguishable from no correction, given the gross assumptions used in developing the value of the corrective multiplier.

This multiplier for the Ascension Island data set, however, is 0.84. This is significantly different from 1.0, and is in very good agreement with the value of 0.8 derived from a comparison of the Ascension Island $SI(dB)$ values with published samples of the digital Ascension Island data [Secan, 1991].



Data limited to $-1h < \text{E-region sunset} < +8h$

Figure 1: S_4 distributions from the Kwajalein and Ancon Wideband VHF data sets (top and bottom plots) and derived from the Ascension Island Marisat L-band $SI(dB)$ data set.

Station	Frequency	Satellite	S_4 method	Peak location
Kwajalein	VHF	Wideband	direct	0.93 (+/- 0.025)
Ancon	VHF	Wideband	direct	0.93 (+/- 0.025)
Huancayo	VHF	Marisat	convert from SI	0.98 (+/- 0.05)
Manila	VHF	Fleetsat	convert from SI	0.85 (+/- 0.025)
Kwajalein	L-band	Wideband	direct	insufficient data
Ancon	L-band	Wideband	direct	insufficient data
Huancayo	L-band	Marisat	convert from SI	0.95 (+/- 0.025)
Ascension	L-band	Marisat	convert from SI	1.10 (+/- 0.025)

Table 2: Location of peaks in S_4 distribution plots.

In the second approach, personnel at PL/GPIA analyzed a small sample of digital intensity data collected at Ascension Island and calculated both S_4 and $SI(dB)$ from the same 15-minute samples. These data were fit with an equation in the same form as Equation [1] relating S_4 to $SI(dB)$, which resulted in the following relationship:

$$S_4 = 0.0764SI(dB)^{0.72} \quad (2)$$

Figure 2 shows the relationship between $SI(dB)$ and S_4 from the original Whitney algorithm (dotted line), from the fit to the Ascension Island digital data (solid line), and from the Whitney algorithm modified with the multiplier of 0.84 derived from the S_4 distributions (dashed line). The agreement between the results obtained from the digital data and that from the comparison of the S_4 distributions is excellent.

As a result of these analyses, we have decided to use the Whitney algorithm modified by the multipliers derived from the locations of the peaks in the S_4 distributions to convert $SI(dB)$ to S_4 . We have not attempted to determine why the unmodified Whitney algorithm did not work correctly, nor why the adjustment factors are different at the different stations (and for different frequencies). It is possible that these factors represent calibration factors which are required to bring the various measurements into relative agreement with one another. It is enough for our purposes that the adjustment agrees with an algorithm derived directly from the data in the one case for which the data are available (Ascension L-band), and that we apply it consistently across our data sets.

2.2 Database Design. The equatorial database files designed to facilitate the WBMOD model validation conducted in 1991 are large and cumbersome, and they do not lend them-

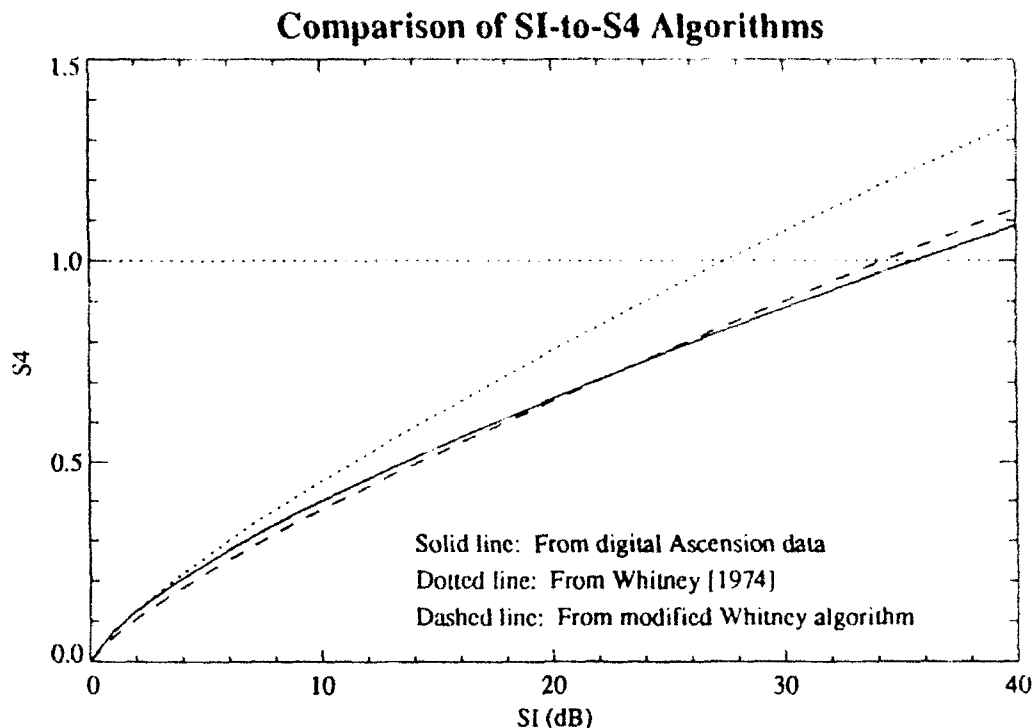


Figure 2: Comparison of algorithms for converting $SI(dB)$ to S_4 .

selves to the types of studies envisioned for the modeling process. We have redefined the layout of the equatorial database tailored to the types of modeling we expect to do and the parameters we expect to require for modeling.

The validation database stored each observation as an independent entity. This leads to a somewhat disjoint database and quite a bit of data duplication (both implicitly and explicitly). We reformatted the databases provided by Phillips Lab (Huancayo, Manila, Ascension Island) so that the data are stored in data blocks which will include 24 hours of data to include the $SI(dB)$ observations as well as parameters to be used in the modeling. Figure 3 is a listing of the design of a data structure for this new database. A single data structure contains the $SI(dB)$ values for a 24-hour period starting with the first value after local solar noon on a given day. Definition of each element is as follows:

INTSEC0	Date/time of first $SI(dB)$ value (seconds)
SI(96)	$SI(dB)$ values for the 24-hour period
ELT0	Time since E-layer sunset of first $SI(dB)$ value (hours)
TPSS0	Time since E/F2-layer sunset of first $SI(dB)$ value (hours)
DOY	Day of the year (GMT) of first $SI(dB)$ value
PHITRM	Angle between sunset terminator and the geomagnetic meridian
KP(9)	K_p values covering the 24-hour period
KP_SS	K_p value at E/F2 sunset

```

STRUCTURE /DATA_RECORD/
  INTEGER INTSEC0
  REAL    SI (96)
  REAL    ELT0
  REAL    TPSS0
  REAL    DOY
  REAL    PHITRM
  REAL    KP (9)
  REAL    KP_SS
  REAL    SUM6_KP_SS
  REAL    DST (25)
  REAL    DST_MIN
  REAL    SLT_DST_MIN
  REAL    AVE_DST_DAY
  REAL    AVE_DST_PSS
  REAL    AVE_DST_PM
  REAL    SSN
  REAL    SSN_5
  REAL    SSN_90
  REAL    F10
  REAL    F10_5
  REAL    F10_90
  REAL    SPARES (2)
END STRUCTURE

```

Figure 3: Database structure for data from Ascension Island, Huancayo, and Manila.

SUM6_KP_SS	$\sum K_p$ for six-hour period prior to E/F2-layer sunset
DST(25)	D_{st} values covering the 24-hour period
DST_MIN	Minimum D_{st} observed during the 24-hour period
SLT_DST_MIN	Local solar time (LST) of D_{st} minimum (hours)
AVE_DST_DAY	Average D_{st} between local noon and E/F2 sunset
AVE_DST_PSS	Average D_{st} between E/F2 sunset and local midnight
AVE_DST_PM	Average D_{st} between local midnight and 0600 LST
SSN	Sunspot number (SSN)
SSN_5	Five-day mean SSN
SSN_90	90-day mean SSN
F10	10.7 cm solar radio flux (F_{10})
F10_5	Five-day mean F_{10}
F10_90	90-day mean F_{10}
SPARES(2)	Unused space for future use

Note that the Wideband data sets from Ancon and Kwajalein were kept in the form used in the validation. These data are from individual satellite passes, and the database format used in the validation is better for this type of data than the new format. We will also retain the validation format for the high-latitude modeling for the same reason.

The various geomagnetic-activity parameters included in this list, such as the various average D_{st} values, are based on our literature review to date. They were selected to provide parameters which would reflect observed behavior, such as in *Aarons [1991]*, and theoretical modeling, such as in *Kelley and Maruyama [1992]*, reported in the literature.

3. Irregularity Models Development

3.1 Model for $\log(C_k L)$ PDF. From its inception, the WBMOD model has dealt strictly with the mean of the $C_k L$ distribution. While this treatment is reasonable for mid and high latitudes where the $\log(C_k L)$ distribution is very nearly normal (i.e., the distribution is well represented by a Gaussian curve), recent studies have shown that it is not adequate for representing conditions in the equatorial post-sunset regime (*Secan and Fremouw [1988]*). As shown in Figure 4, the distribution of $\log(C_k L)$ in this regime is rather more bimodal than normal, which leads to the situation where the mean of the distribution is not representative of the distribution. In addition, characterizing only the mean of the distribution does not allow for providing model users with statistics which may be of use to them such as generation of 95th-percentile values for worst-case estimates or the percent of the time that scintillation levels will exceed a user-defined threshold.

In the previously cited study, it was found that the $\log(C_k L)$ distributions observed at all latitude regimes (equatorial, mid latitude, auroral, and polar cap) could be modeled using a linear combination of Gaussian functions. In all but the equatorial-night case, only a single function was required. In the equatorial-night case (as in Figure 4), the distribution could be adequately modeled by a three-component PDF.

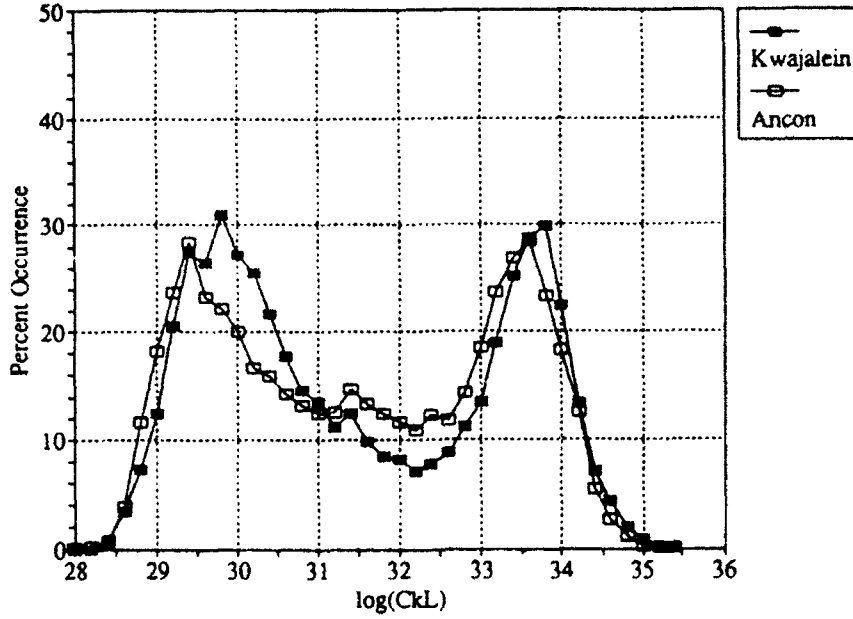


Figure 4: Distribution of $\log(C_k L)$ during the post-sunset period at Kwajalein and Ancon from the Wideband experiment (VHF).

The functional form of the model to be used for the $\log(C_k L)$ probability distribution function (PDF) will be a composite function consisting of two gaussian peaks joined together by a "top hat" function which has a fixed value between the peaks and is zero outside this range. The functional form is given by

$$PDF = \sum_{i=1}^2 (\eta_i - \eta_p) \exp \left[- \left(\frac{\log(C_k L) - \mu_i}{\sigma_i} \right)^2 \right] + \eta_p \quad (3)$$

$$\eta_p = \begin{cases} \eta_3 & \text{if } \mu_1 \leq \log(C_k L) \leq \mu_2 \\ 0 & \text{elsewhere} \end{cases} \quad (4)$$

where $(\mu_i, \sigma_i, \eta_i; i = 1, 2)$ define the $\log(C_k L)$ values, the half-widths, and the distribution-peak values for the two peaks, and η_3 is the value of the "top hat" segment of the model. After the various regional models are used to determine values for these seven parameters, the resulting PDF is normalized so that it integrates to 1.0 (i.e., $CDF[\log(C_k L) \rightarrow \infty] \rightarrow 1.0$). Figure 5 is an example of a PDF and the corresponding CDF constructed using this new model formulation. It can be compared with the actual distributions shown in Figure 4.

The modeling now to be completed will describe the variation of these seven parameters as functions of location, time, and geophysical conditions.

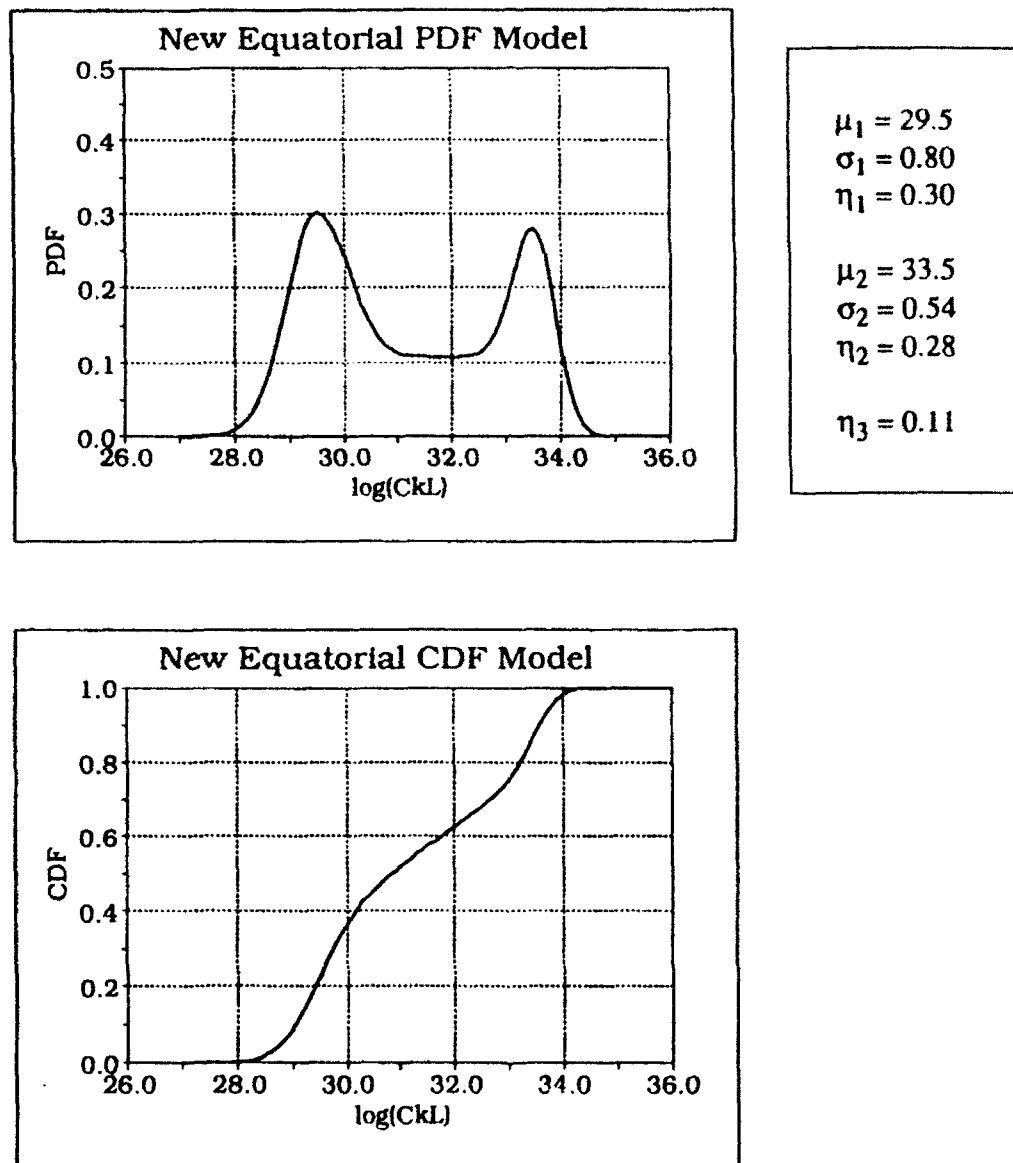


Figure 5: Probability distribution function (PDF) (top plot) and cumulative distribution function (CDF) (bottom plot) for an equatorial station. These were generated using the new three-component PDF model (see text) with the parameters indicated in the side box.

3.2 Modeling Philosophy. As we began to analyze the data to extract the variations in the seven parameters described above, it became evident that we would need to alter the way in which we have developed the parameters for the WBMOD $C_k L$ model in the past (see *Robins et al.* [1986] and *Secan* [1989] for discussions of previous procedures). Several factors have motivated this change:

1. We are now modeling the full distribution of $\log(C_k L)$ rather than simply the mean of the distribution. Thus, there are far more *interrelated* parameters to deal with.
2. Intensity scintillation, which makes up the majority of the data to be used, saturates at a level which is frequency-dependent. In addition, the hand-scaled SI(dB) data have artificial "quantization" effects near the noise floor (the location of which is also frequency dependent). These two effects make it impossible to extract the parameters required directly from S_4 (or $\log S_4$) PDFs.
3. Due to the range-limited nature of the intensity scintillation data (i.e., noise-floor at the low end and saturation at the high), it can be difficult to determine whether an increase in the number of observations near the top of the S_4 distribution is caused by an increase in the population in the plume distribution (an increase in η_2) or an increase in the $\log(C_k L)$ value at the peak (an increase in μ_2).

After much trial and error, we have come up with the following procedures and "rules of thumb" for the modeling effort:

1. The half-widths of the two gaussians, σ_1 and σ_2 , will be set at values derived from examination of the $\log(C_k L)$ PDFs generated from the WIDEBAND σ_ϕ data sets. Since the phase scintillation does not saturate at high levels of $C_k L$, these data provide the best picture of the shape of the higher post-sunset gaussian peak associated with plume structures. In addition, since the WIDEBAND data were machine processed rather than hand scaled and are available at a lower frequency (137 MHz), they also provide a better picture of the shape of the lower gaussian peak.
2. The $\log(C_k L)$ of the lower gaussian peak, μ_1 , will also be taken from the WIDEBAND VHF data set for the reasons stated in the last sentence of the previous paragraph.
3. In order to determine whether to increase η_2 or μ_2 (as in item #3 above), we will follow the simple rule of thumb that if we believe that the variation being studied should result in an increase in ΔN , we will model the variation by changing μ_2 . If we believe that the variation is related to the probability of the existence of a plume structure, we will model the variation by changing η_2 . We have tried to hold to this rule as much as possible, although it is sometimes difficult to decide which of these two cases are being dealt with.

4. Since the η_i values of the resulting PDF are to be normalized so that the PDF integrates to unity, we will set the value of η_1 to a fixed value and model changes in the relative sizes of the upper and lower populations by altering the value of η_2 . In order to simplify the modeling effort, we have also decided to set the value of the "top hat" segment of the model, η_3 , to a fixed percentage of η_2 .
5. The modeling will be conducted by comparing contour plots of the percent of the time that S_4 exceeds two threshold values (0.5 and 0.8 for all but the Huancayo L-band data; 0.15 and 0.25 for Huancayo L-band) as generated from the various data sets and as generated from the model. In as many cases as possible, the contour plots will be a function of GMT along the x-axis and day of the year along the y-axis. Figure 6 is an example of such a plot from the Manila data set. The constants of the models developed to describe the variations of the various PDF parameters will be iteratively adjusted to provide visual best fits to the entire data set.

As stated in item #3, we have tried to follow these rules and procedures as much as possible, although some deviations have been required. Usually, when we have found that a particular rule or procedure was not working well, it was either modified or replaced. The modeling procedure has definitely grown and changed in the course of the modeling effort.

3.3 Latitudinal Variation. The algorithm for the latitudinal variation of $C_k L$ across the equatorial region in the current WBMOD model is a very simple one, which does not allow for higher $C_k L$ values near the crest of the anomaly region than at the equator. In order to allow for this sort of variation with latitude, we will need to replace this algorithm with one which will permit this sort of behavior. The current model specifies $C_k L$ in the mid-latitude region and at the geomagnetic equator, then uses a simple error function to transition from one to the other across a specified boundary latitude with a specified transition width. The new algorithm will be similar, but will add gaussian-shaped peaks at the poleward edges of the equatorial region (north and south) which are defined by a new set of model constants.

The form of the new latitudinal algorithm is as follows:

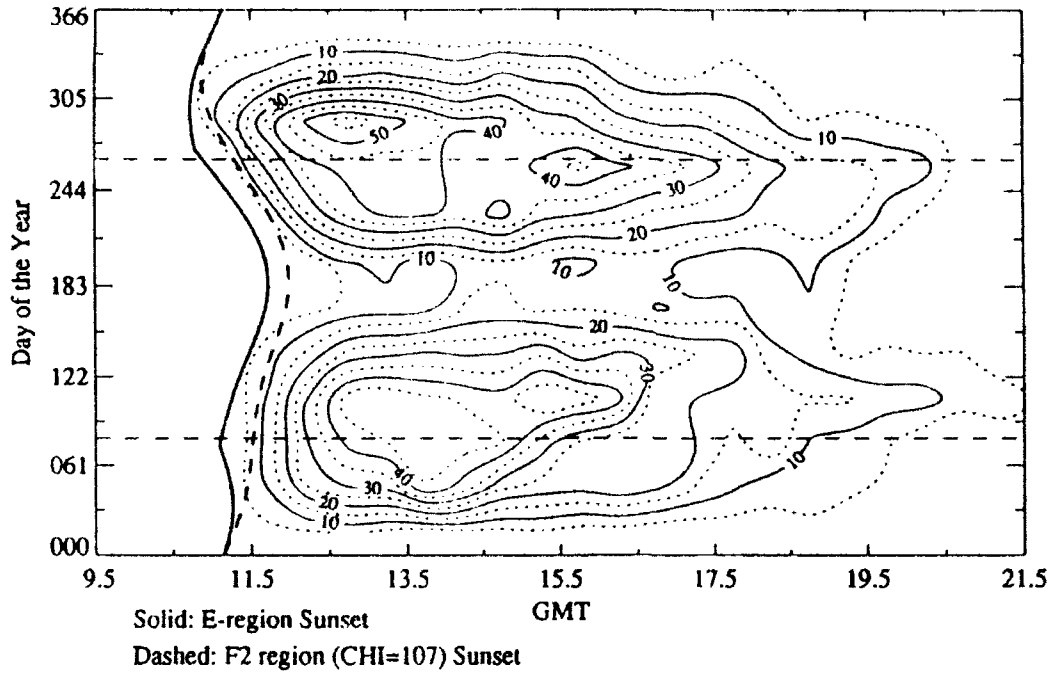
$$\log(C_k L) = C_0 + (C_C - C_0) \exp \left[- \left(\frac{|\lambda_a| - \lambda_C}{W_C} \right)^2 \right] \quad (5)$$

$$C_0 = \begin{cases} 0 & |\lambda_a| > \lambda_C \\ C_{E0} & |\lambda_a| \leq \lambda_C \end{cases}$$

$$C_C = \begin{cases} C_{CN} & \lambda_a \geq 0 \\ C_{CS} & \lambda_a < 0 \end{cases}$$

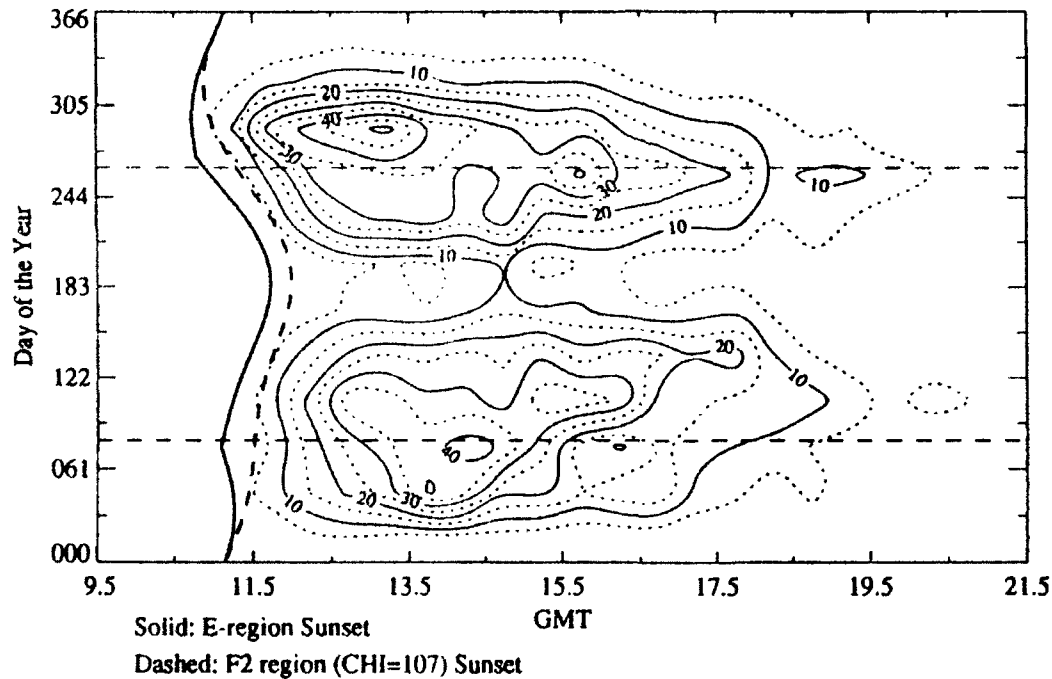
Manila-FLEETSAT (VHF)

Percent of Time $S_4 > 0.5$



All SSN
Kp ≤ 2.0
Total Points: 28,621
Points > 0.5 : 3,335

Percent of Time $S_4 > 0.8$



All SSN
Kp ≤ 2.0
Total Points: 28,621
Points > 0.8 : 2,349

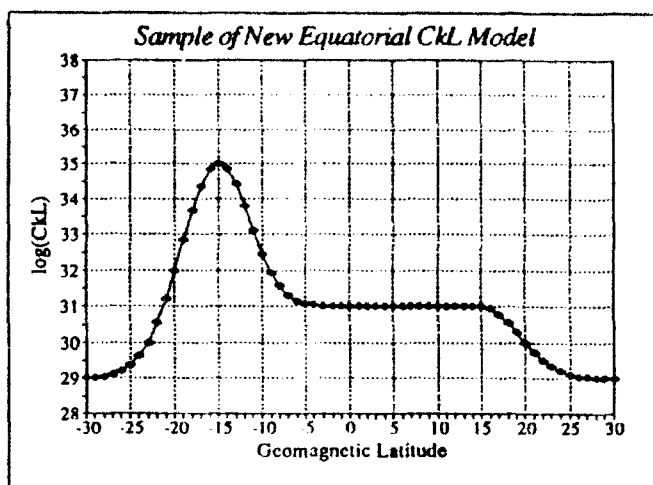
Figure 6: Contour plots of the percent of time that S_4 exceeds 0.5 (upper plot) and 0.8 (lower plot) as a function of GMT and day of the year from the Manila-FLEETSAT UHF database. The horizontal dashed lines indicate the equinoxes, the heavy solid and dashed lines indicate the time of E-region sunset (both E-region ends of the field line are in sunset) and F2-region sunset (solar declination, χ , is 107°).

$$W_C = \begin{cases} W_N & \lambda_a \geq \lambda_C \\ W_E & |\lambda_a| \leq \lambda_C \\ W_S & \lambda_a \leq -\lambda_C \end{cases}$$

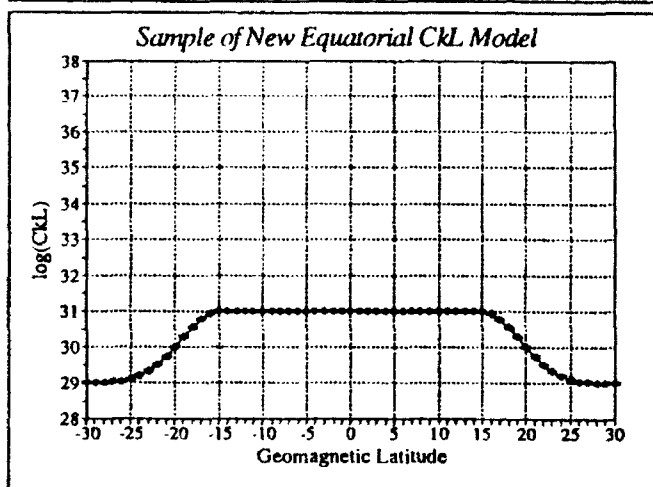
where λ_a is the geomagnetic (modified apex) latitude; C_{E0} is the equatorial value of the parameter varied; C_{CN} and C_{CS} are the maximum values of the parameter varied in the northern and southern anomaly crest regions; λ_C is the geomagnetic latitude of the anomaly maxima (always positive); and W_N , W_E , and W_S are the e-folding widths of the gaussian features north of $+\lambda_C$, equatorward of $\pm\lambda_C$, and south of $-\lambda_C$. All of these parameters may vary as functions of other variables such as time of day or season, although it is likely that at least a few (such as the transition widths) will either be fixed or will vary as simple functions of the other parameters. Figure 7 shows three examples of the latitude variations possible with this formulation.

We have placed the following initial constraints on the modeling effort:

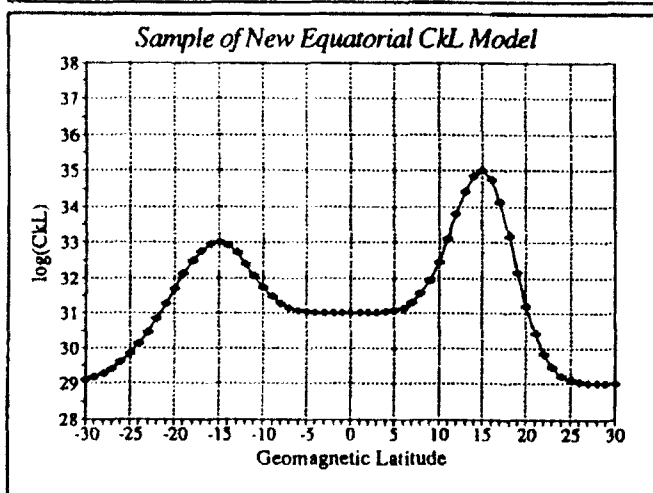
1. Only the $\log(C_k L)$ value of the upper peak in the PDF, μ_2 , will be varied with latitude. This is tantamount to assuming that the increase in scintillation activity levels observed near the anomaly crest (at Ascension Island, in the present data set) is due to increased levels of ΔN . Since this has been the primary argument for the increase (i.e., there is more plasma (N) available at the anomaly crest than on the equator, therefore ΔN can be higher at the crest), we felt that this was a reasonable first assumption. [As we will see in a later section, this had to be modified slightly.]
2. The maximum values in μ_2 will occur at apex latitude $\pm 16^\circ$ with a latitude half-width of 5° on each side of the peak. The location of the peak was selected to coincide with the latitude of Ascension Island, the only data in the set near the crest, and the width was selected to reduce to the equatorial value by the latitude range covered by the Wideband data sets, which showed no latitude variation in $C_k L$.
3. The latitude variation will be assumed identical in all longitude sectors. We have some reservations about this assumption based on studies that have shown that the higher scintillation levels observed at Ascension may have a longitude component as well as a latitude one (see *Basu et al.* [1976] and *Maruyama and Matuura* [1984]), but as we have no other scintillation data set near the crest from another longitude sector, we must assume (for now) that the differences in observed scintillation levels at Huancayo and Ascension Island are representative of the latitude variation at all longitude sectors. Note, however, that this is *definitely* an area that needs further study with a more extensive data set.
4. We will assume (at least initially) that the maximum $C_k L$ observed at Ascension corresponds to the $\log(C_k L)$ calculated from an SI(dB) value of 30.0 (36.0), which is at the top end of the SI(dB) distribution from that station. Due to the saturation effect found in intensity scintillation, this could well be low. However, we have no



$\lambda_c = 15^\circ$
 $C_kL_{M0} = 29.0$
 $C_kL_{E0} = 31.0$
 $C_kL_{CN} = 31.0$
 $C_kL_{CS} = 35.0$
 $W_N = 6.0$
 $W_E = 5.0$
 $W_S = 6.0$



$\lambda_c = 15^\circ$
 $C_kL_{M0} = 29.0$
 $C_kL_{E0} = 31.0$
 $C_kL_{CN} = 31.0$
 $C_kL_{CS} = 31.0$
 $W_N = 6.0$
 $W_E = 5.0$
 $W_S = 6.0$



$\lambda_c = 15^\circ$
 $C_kL_{M0} = 29.0$
 $C_kL_{E0} = 31.0$
 $C_kL_{CN} = 35.0$
 $C_kL_{CS} = 33.0$
 $W_N = 5.0$
 $W_E = 5.0$
 $W_S = 8.0$

Figure 7: Samples of the new equatorial C_kL model formulation. The model parameters used in each are defined in the adjacent boxes. See the text for a description of the model and model parameters.

evidence to set $\log(C_k L)$ higher. This would require SI(dB) observations from a higher frequency, or phase scintillation observations at L-band or higher.

Thus, we are specifying only the values for μ_2 at the dip equator and at the anomaly crest. We will use the maximum $\log(C_k L)$ from the Ascension Island set as the value at the crest, and a value of 33.5 at the dip equator. This last value was initially taken from the average value of the $\log(C_k L)$ peak in the two Wideband data sets [Secan, 1989], and was later found to be in fair agreement with a value extracted from the Huancayo UHF and L-band data sets.

3.4 Diurnal Variation. The first issue to resolve in modeling the diurnal variation, a variation dominated by the rapid onset of intense scintillation just after local sunset, was to select the time metric to use in the model. The current WBMOD equatorial $C_k L$ model uses the time since sunset has occurred in the E-region at both ends of the field line passing through the ionospheric penetration point (IPP). This time metric, which we will denote ERSS (for E-region sunset), was based on the hypothesis by Tsunoda and Wittwer (Tsunoda [1985]) that the field-line integrated Pedersen conductivity was a major controlling factor in the onset and growth of the instabilities that develop into post-sunset plumes. This parameter is largely determined by the electron density at the E-region ends of a particular field line, and the conductivity drops to nearly zero shortly after both E-region ends of the field line have passed through the sunset transition.

The development of the diurnal variation in the WBMOD equatorial $C_k L$ model was severely limited by the fact that the data available for the modeling work (Wideband data from Ancon and Kwajalein) were limited to a two-hour period centered at 4.0 ERSS at Ancon and a ninety-minute period centered at 4.5 ERSS at Kwajalein (see Figure 14 in *Fremouw and Robins* [1985]). The data sets provided by PL/GPIA cover the full 24 hours, which will allow us to improve this section of the model. In fact, an initial improvement was made based on the Ascension Island data during the model validation (see page 4 in *Secan* [1991]).

The plots in Figures 8 through 12 show the diurnal behavior of the SI data from Ascension Island (Marisat, L-band and VHF), Manila (Fleetsat, VHF), and Huancayo (Marisat, VHF and L-band), as a function of GMT and day of the year. These figures are contour plots of the percent of time that SI exceeded a particular threshold (3 dB for Huancayo L-band, 10 dB for the other sets) as a function of GMT and the day of the year for an eight-hour time segment beginning near local sunset. The heavy solid line on each plot is the time of E-region sunset as defined above (i.e., $ERSS = 0.0$), and the heavy dashed line is the time of sunset in the F2 region. (This last time will be denoted F2RSS, so the heavy dashed line is at $F2RSS = 0.0$.) These times are calculated at locations to be defined later. It is apparent from the data that the onset of scintillation lags the $ERSS=0$ time, and appears to track fairly well with a combination of the two sunset times.

The decision to include the $F2RSS=0$ line in these plots was based on recent work by *Maruyama* [1988] and *Kelley and Maruyama* [1992], in which a physical model for the growth

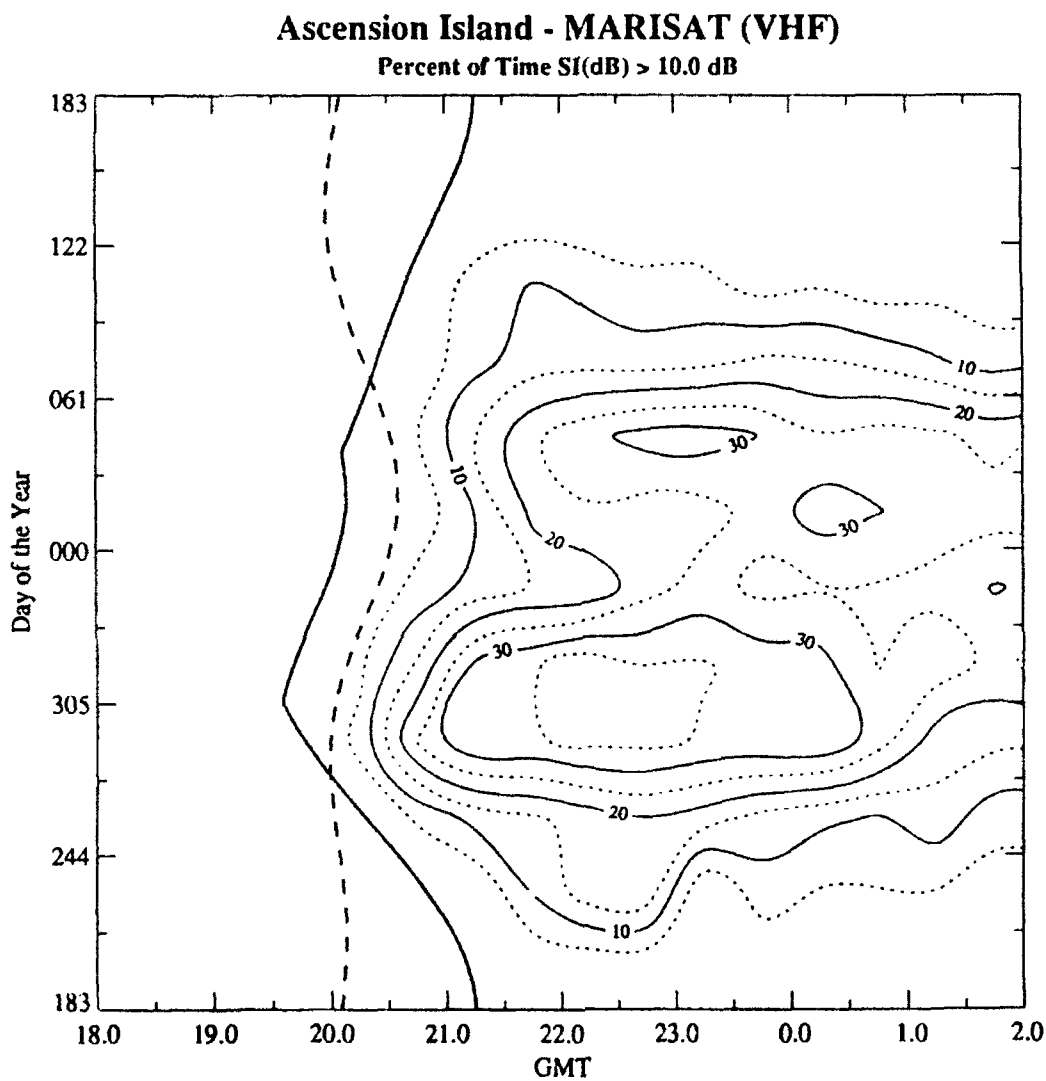


Figure 8: Diurnal behavior of intensity scintillation from the Ascension Island Marisat (VHF) data set. Contours of the percent of the time that SI exceeded 10 dB are plotted as a function of GMT and the day of the year. The heavy solid line shows the variation of $ERSS = 0$ with the day of the year, and the heavy dashed line shows the variation of $\chi = 107^\circ$.

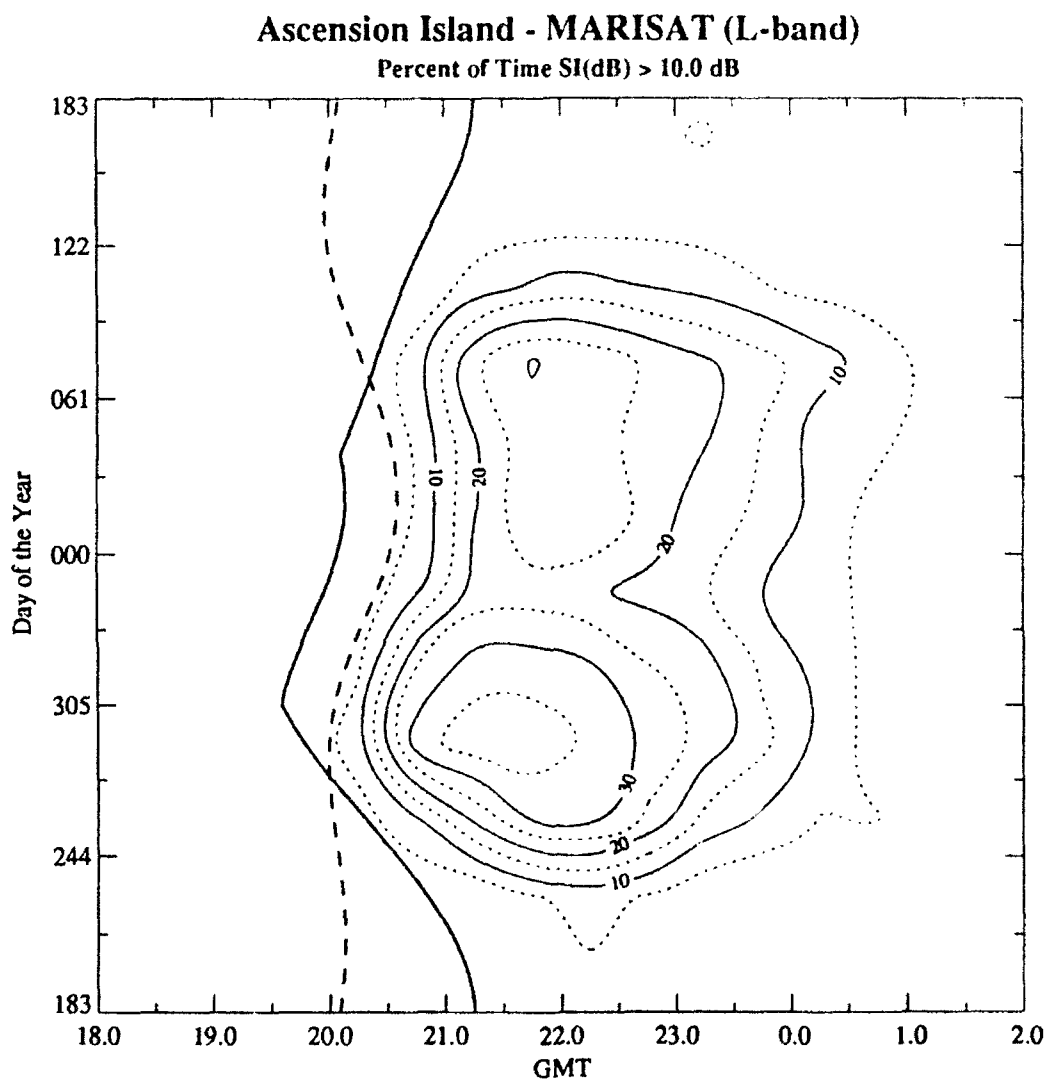


Figure 9: Diurnal behavior of intensity scintillation from the Ascension Island Marisat (L-band) data set. Contours of the percent of the time that SI exceeded 10 dB are plotted as a function of GMT and the day of the year. The heavy solid line shows the variation of ERSS = 0 with the day of the year, and the heavy dashed line shows the variation of $\chi = 107^\circ$.

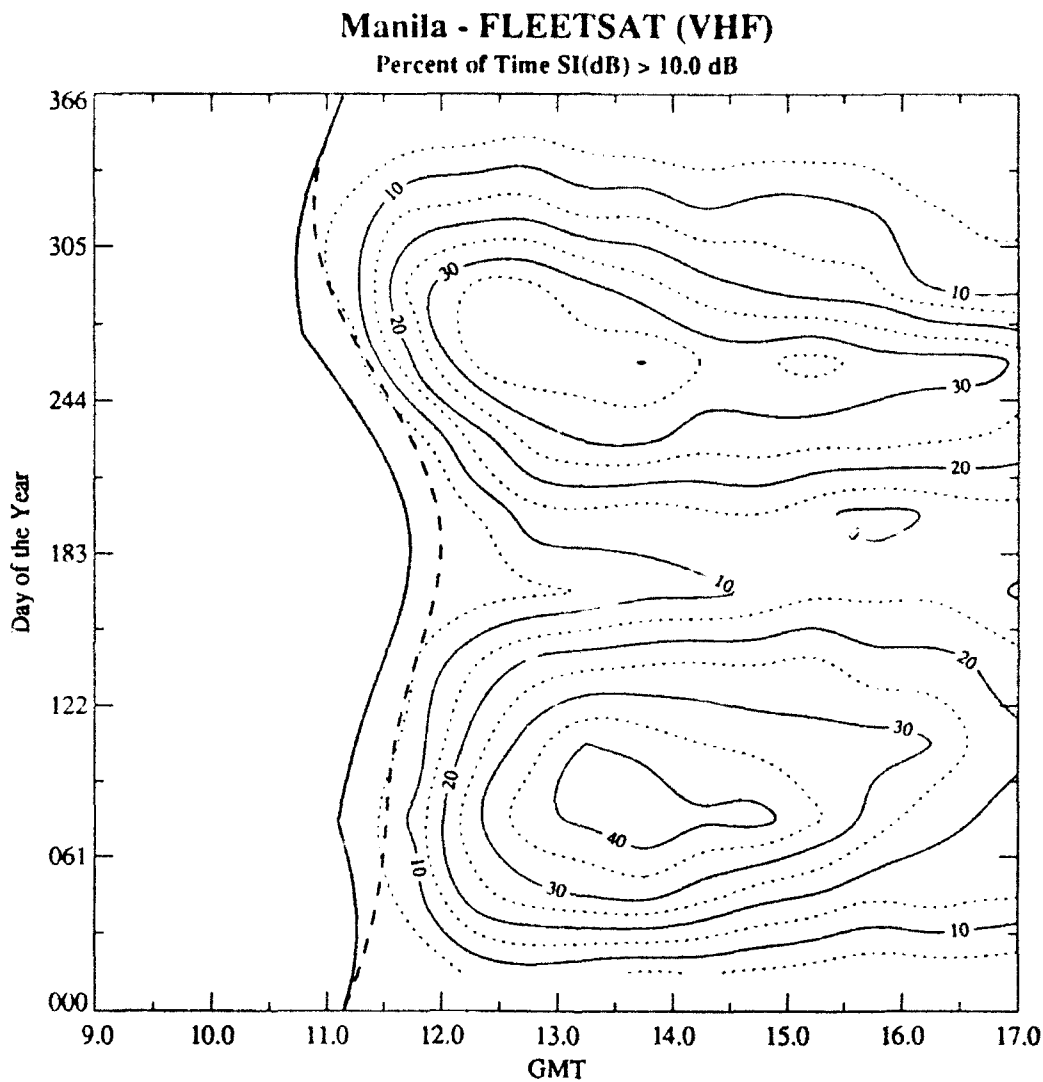


Figure 10: Diurnal behavior of intensity scintillation from the Manila Fleetsat (VHF) data set. Contours of the percent of the time that SI exceeded 10 dB are plotted as a function of GMT and the day of the year. The heavy solid line shows the variation of $ERSS = 0$ with the day of the year, and the heavy dashed line shows the variation of $\chi = 107^\circ$.

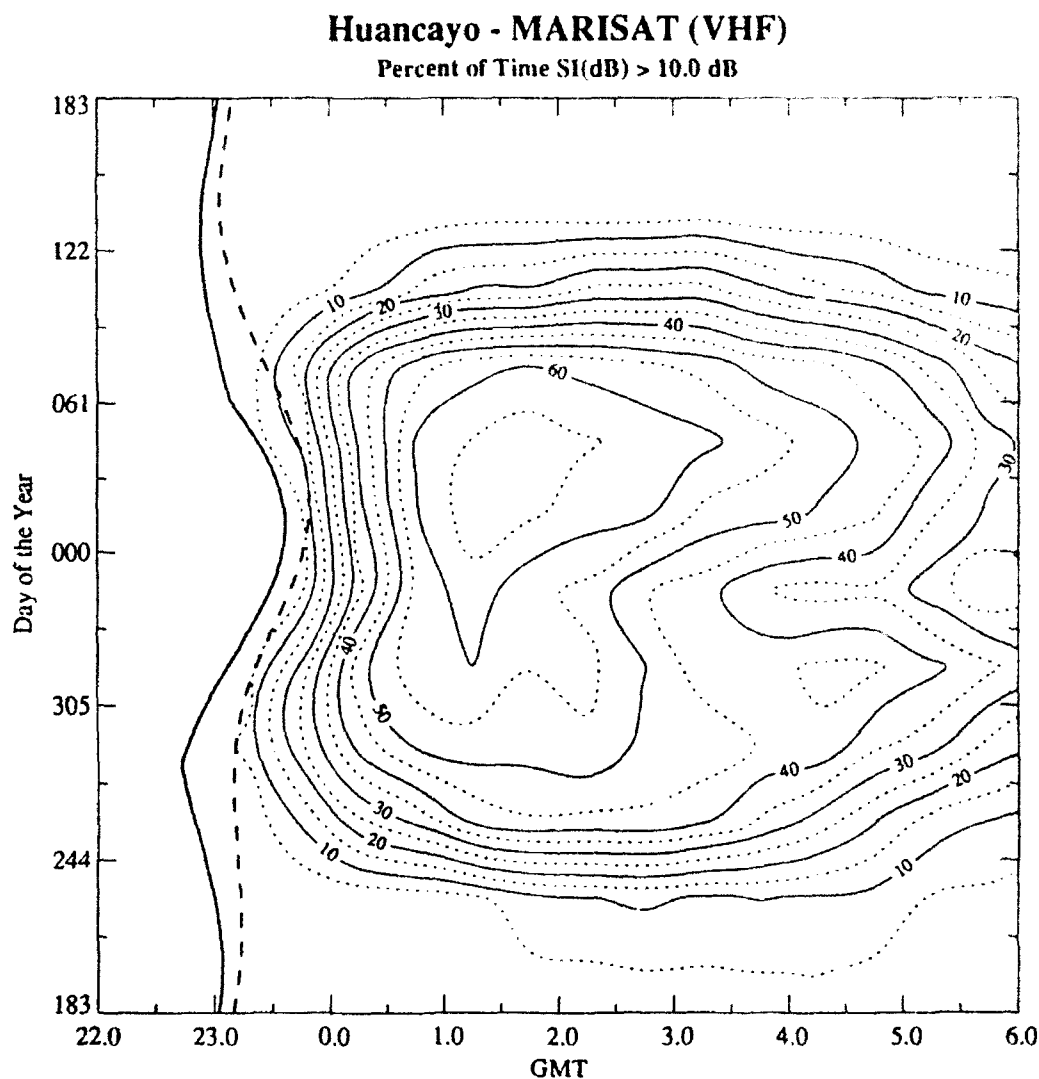


Figure 11: Diurnal behavior of intensity scintillation from the Huancayo Marisat (VHF) data set. Contours of the percent of the time that SI exceeded 10 dB are plotted as a function of GMT and the day of the year. The heavy solid line shows the variation of $ERSS = 0$ with the day of the year, and the heavy dashed line shows the variation of $\chi = 107^\circ$.

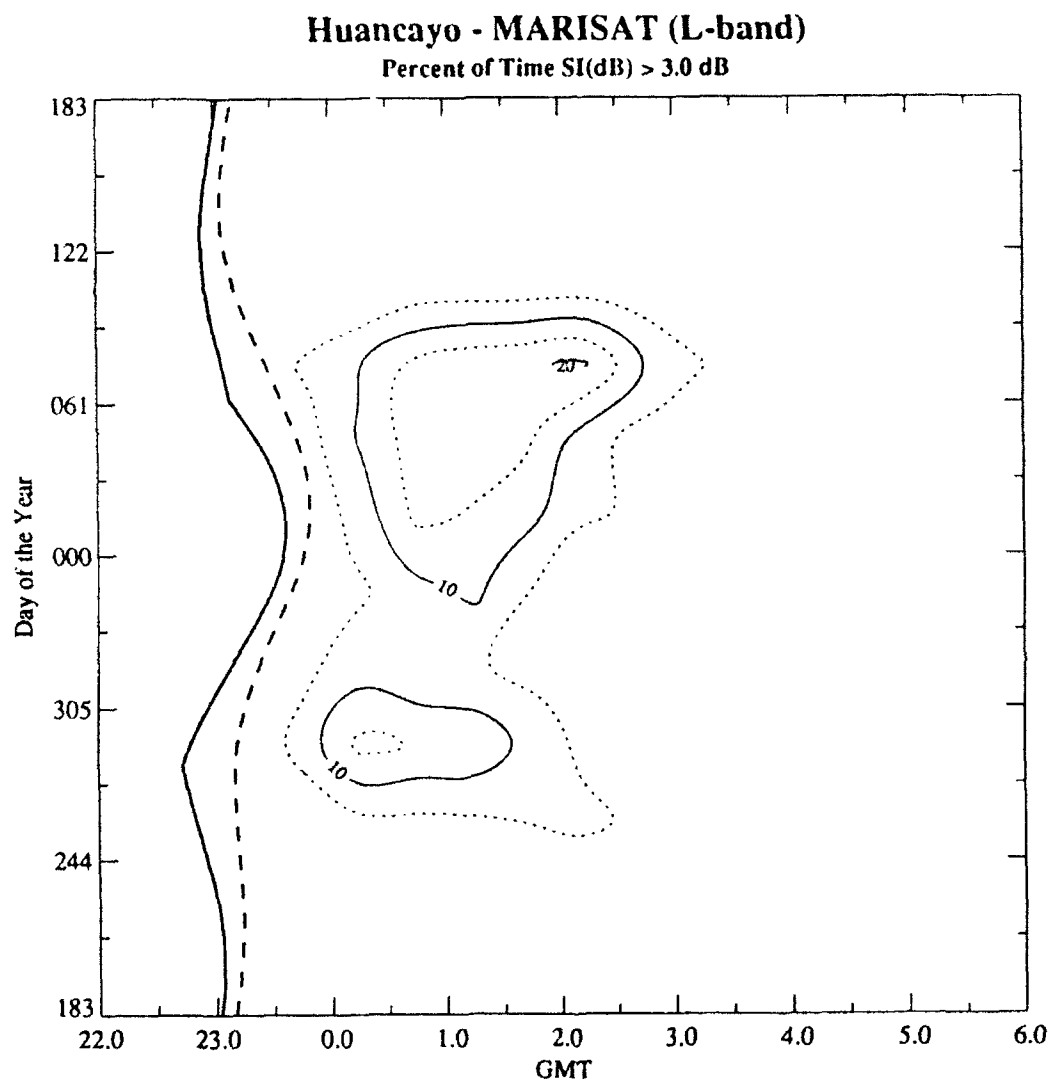


Figure 12: Diurnal behavior of intensity scintillation from the Huancayo Marisat (VHF) data set. Contours of the percent of the time that SI exceeded 10 dB are plotted as a function of GMT and the day of the year. The heavy solid line shows the variation of ERSS = 0 with the day of the year, and the heavy dashed line shows the variation of $\chi = 107^\circ$.

of post-sunset plume structures was developed. This model indicates that photoionization in the F2 layer is an important "brake" on the growth process, and that the growth rate increases as photoionization in the F2 layer decreases at sunset. Thus, as our initial time metric, we have chosen a sunset time for onset of plume-structure development which is a combination of the E- and F2-region sunsets described earlier. This time, denoted t_e is defined as the time since the later of ERSS=0 or F2RSS=0. In referring to Figures 8 through 12, t_e is F2RSS on those days when the dashed line is to the right of the solid line and is ERSS when the relative positions are reversed. For Ascension Island, F2RSS controls the process from roughly the autumnal equinox to the vernal equinox, and ERSS controls for the rest of the year. At the other two stations, the F2RSS controls for the entire year.

In our initial modeling, we used our standard method of specifying conditions at an ionospheric penetration point (IPP) for calculating the various sunset times. The ERSS and F2RSS times calculated for Huancayo using this method resulted in the scintillation onset preceeding the sunset times by as much as 20 to 30 minutes. (Note that the time lines plotted on Figures 11 and 12 were calculated using the new procedure.) This early onset was a concern for a while, but it was eventually resolved in principle if not in detail. In a recent paper, *Mendillo et al.* [1992] showed two sets of east-west scans from the Altair radar located at Kwajalein on two nights in August 1988. These scans showed several examples of the plume structures that are the source of the most severe post-sunset scintillation events. In particular, the scan from 07:57 UT on 14 August (their plate 1a) shows an intense plume structure located at the eastern boundary of the scan, and the scan from 08:30 UT on 15 August (plate 1b) shows a plume structure located just east of the radar. The scans just prior to both of these (9 minutes prior on 14 August, 35 minutes on 15 August) were devoid of plume signatures. There are two observations that can be made about these plumes that are germane to the question at hand (timing at Huancayo):

1. Both plumes extend well above the sunset terminator, defined as a line passing from the center of the sun tangent to the earth's surface. A consequence of this is that a receiver "looking" eastward at a low elevation angle (such as the Huancayo-Marisat geometry) can encounter irregularities in the topside ionosphere prior to the terminator crossing the line of sight at ionospheric altitudes.
2. In the non-plume scans, the local time at the location where the plume develops in the next scan is past the E-region sunset time but prior to the F2 sunset time. In the plume scans, the local time at the plume location is after the F2 sunset time. This is in accord with the hypothesis discussed earlier that the plumes would develop after both the E and F2 sunset times.

This provides additional information that may allow us to explain and model the variation in onset times at the three stations.

The F2 sunset time preceded the plume scan on 15 August by only one minute. This is not enough time for the plume to have developed fully to a height of over 800 km (assuming

a start at a height of 400 km, this would require a vertical rise velocity of almost 7 km/s). It would appear that the time that photochemistry in the F2 layer no longer can suppress the growth of the instability requires redefinition. If we use the nine-minute spacing between the two scans on 14 August as a bound and parameterize the F2-layer control by the local solar zenith angle, then we find that a solar zenith angle of about 107° corresponds to the earliest time that the plume could have started developing in the 14 August case.

Modeling the onset time will require consideration of the vertical extent of the plumes rather than continue to work solely with geometries calculated for the phase-screen penetration point. The geometry at the three stations (Ascension, Huancayo, and Manila) are well suited to investigating this issue, as the propagation paths are quite different at each station. At Ascension, the azimuth angle of the raypath is nearly along the geomagnetic meridian at a high elevation angle; at Huancayo, the azimuth is eastward (looking towards the approaching sunset terminator) at a low elevation angle; and at Manila, the azimuth is westward (looking away from the terminator), also at a relatively low elevation angle.

The model we have settled on for the zero point of the time metric to be used in the equatorial region will be the time that the E-region points along the field line passing through the equatorial control point (definition to follow) are in darkness after sunset and the solar zenith angle at the latitude/longitude of the control point is $> 107^\circ$. This time metric will be denoted t_e . The equatorial control point is determined as follows:

1. Calculate the UT of sunset ($t_e = 0$) at the latitude/longitude where the line of sight from the receiver to the satellite crosses altitudes defined as the base and top of plume-generated irregularities.
2. The equatorial control point is the one of these two locations with the earliest UT sunset time.
3. The field line along which the E-layer sunset times are calculated is that which passes through the equatorial control point at the base altitude of the plume (as in (1) above).

Thus, we are now defining the time in terms of the intersection of the line of sight with a vertical "wall" of irregularities located along the sunset terminator rather than with the intersection with a horizontal phase screen. We have selected altitudes of 350 km and 800 km for the base and top of the plume "wall" based on qualitative comparisons with the Manila and Huancayo data sets, respectively.

We decided to retain the basic functional form of the diurnal variation used in the present version of WBMOD: a steep rise just after sunset as defined above using a gaussian function, a short-duration flat-top peak, and a more gradual decrease throughout the night using a second gaussian function. We will deconvolve the two gaussian segments the sunset and sunrise segments. The actual form used is as follows:

$$f(t_e) = \begin{cases} \exp \left[- \left(\frac{t_e - t_{ss}}{W_{ss}} \right)^2 \right] & \text{if } t_e < t_{ss} \\ 1.0 & \text{if } t_e \leq t_e \leq t_{sr} \\ \exp \left[- \left(\frac{t_e - t_{sr}}{W_{sr}} \right)^2 \right] & \text{if } t_e > t_{sr} \end{cases} \quad (6)$$

where t_e is the time past sunset, t_{ss} and W_{ss} are the peak time and half-width of the post-sunset gaussian, t_{sr} is the time at which the "sunrise" segment of the variation starts its decrease, and W_{sr} is the half-width in the sunrise segment. The diurnal variation for any particular parameter is then given by

$$x = x_{day} + (x_{day} - x_{night})f(t_e) \quad (7)$$

where x_{day} is the daytime value and x_{night} is the maximum nighttime value.

We found in modeling that, while the observed variations could be best fit by using the variation modeled in Equation [6] for the σ_i and η_i parameters, the observed rapid onset of severe scintillation that is occasionally observed at all stations could not be adequately modeled unless the μ_2 parameter (the $\log(C_k L)$ value of the plume-associated peak in the PDF) was set to its maximum value immediately upon crossing the sunset line. In order to model this, we have set the diurnal variation function for the two μ_i parameters to the following:

$$f_\mu(t_e) = \begin{cases} 1.0 & \text{if } t_e < t_{ss} \\ 1.0 & \text{if } t_e \leq t_e \leq t_{sr} \\ \exp \left[- \left(\frac{t_e - t_{sr}}{W_{sr}} \right)^2 \right] & \text{if } t_e > t_{sr} \end{cases} \quad (8)$$

This function is then used in place of $f(t_e)$ in Equation [7] for the diurnal variation of the μ_i parameters.

In fitting the model to the observations, which was done using the procedure outlined in Section 3.2, it was found that while the t_{ss} , W_{ss} , and t_{sr} parameters could be set as simple constants, the W_{sr} parameter needed to vary as a function of t_e . We found that the scintillation levels dropped off more rapidly in the early (pre-midnight) evening after the peak than later in the early morning hours. We found that we were unable to use a simple gaussian with a constant half-width parameter. In order to keep the model as simple as possible, W_{sr} is modeled to vary linearly with t_e as follows:

$$W_{sr} = W_{sr0} + \frac{t_c}{dW_{sr}} \quad (9)$$

In addition, we found that this variation was different at the crest (Ascension Island) than near the equator (Huancayo and Manila) so there are different W_{sr0} and dW_{sr} values in the equatorial and anomaly crest sections of the model.

The set of parameters for the diurnal variation is as follows:

t_{ss}	1.50 ^h	
t_{sr}	1.75 ^h	
W_{ss}	0.80 ^h	
W_{sr0}	6.00 ^h	Equatorial
	2.00 ^h	Anomaly Crest
dW_{sr}	2.00 ^h	Equatorial
	1.50 ^h	Anomaly Crest

[Note: The overall results will be shown in Section 3.7.]

3.5 Longitudinal Variation. It was found that in order to reconcile the four near-equator data sets (Manila, 5.8°; Kwajalein, 4.1°; Ancon, 0.9°; Huancayo, 1.6°) a longitudinal variation needed to be included in the $\log(C_k L)$ PDF. This has been included in the model by applying a longitudinal modulation on the η_2 parameter such that the value of this parameter in the vicinity of Manila is a factor of 0.70 times the value in the Kwajalein/Huancayo/Ancon/Ascension sector. The very non-uniform longitudinal coverage of the data set made it impossible to rigorously define this variation, so it has been implemented in the following simple form:

$$\eta_{2,night} = \eta_{max} [0.70 + 0.30f(\phi_\eta)] \quad (10)$$

$$f(\phi_\eta) = \begin{cases} \exp \left[- \left(\frac{\phi_\eta - \phi_1}{\Delta\phi} \right) \right] & \text{if } \phi_\eta < \phi_1 \\ 1.0 & \text{if } \phi_1 \leq \phi_\eta < \phi_2 \\ \exp \left[- \left(\frac{\phi_\eta - \phi_2}{\Delta\phi} \right) \right] & \text{if } \phi_\eta > \phi_2 \end{cases} \quad (11)$$

where ϕ_η is a longitude parameter rotated so that $\phi_\eta = 0$ occurs at a geographic longitude of 100°; ϕ_1 and ϕ_2 are 40° and 320°, respectively (corresponding to 140° and 60° E. longitude); and $\Delta\phi$ is set to 10°. These values were set in order to move the transitions away from the locations where we had data, and were based on review of the results documented in *Basu et al.* [1976] and *Maruyama and Matuura* [1984] from *in-situ* observations.

3.6 Seasonal Variation. Since we are now modeling the full $\log(C_k L)$ distribution, we no longer need an explicit model of the probability of the occurrence of plumes in the post-sunset period. Thus, we will return to the formalism used in WBMOD model version 10H1 for the seasonal variation of the parameters that describe the $\log(C_k L)$ PDF. Following the modeling philosophy described in Section 3.2, the seasonal behavior is modeled via alteration of the magnitude of the upper (plume) peak in the $\log(C_k L)$ PDF (i.e., the η_2 parameter). This follows from the assumption that the seasonal behavior is primarily a change in the probability that plumes will occur.

As in version 10G1, the metric used in modeling the seasonal variation is the angle between the geomagnetic meridian and the sunset terminator, ϕ_{term} , with the maximum activity expected when the two planes defined by the meridian and the terminator are aligned ($\phi_{term} = 0$). The rationale for this is presented in *Robins et. al* [1986]. The functional form of the seasonal modulation of the η_2 parameter is as follows:

$$f(\phi_{term}) = \exp \left[- \left(\frac{\phi_{term}}{W_s} \right)^2 \right] \quad (12)$$

where W_s is one of two constants -- one for local summer (15.0) and one for local winter (12.0). The value of ϕ_{term} is calculated from the magnetic declination angle and the angle to the terminator (calculated from the location of the "true" sun) at the phase-screen penetration point. The determination of whether to use the summer or winter value of W_s is also made at that location.

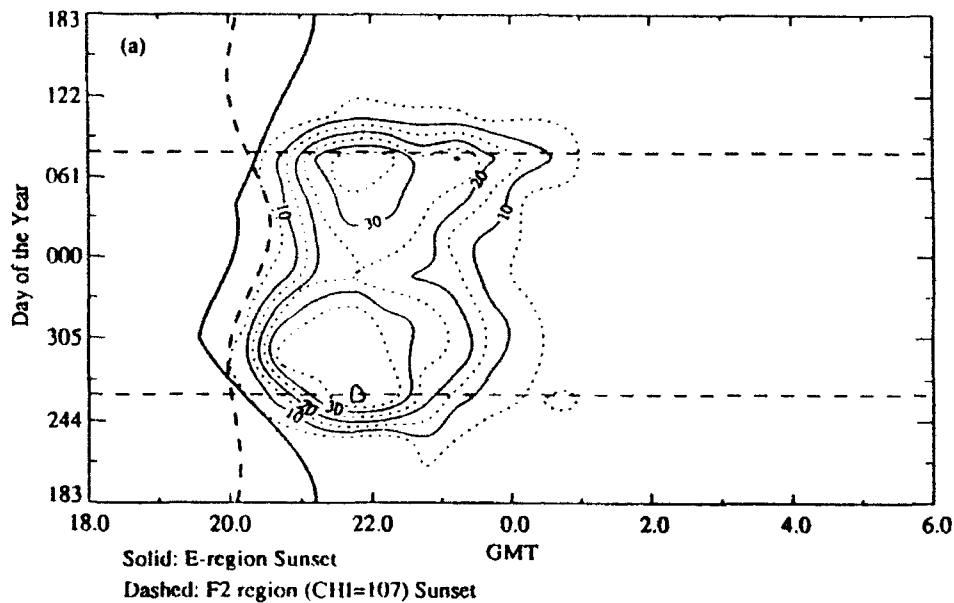
3.7 Results of Diurnal/Seasonal/Longitudinal Modeling. The results of the modeling described in Sections 3.3 through 3.6 are shown in Figures 13-22. These figures are in pairs, with the first figure in each pair showing the diurnal and seasonal variation of the percent of time that S_4 exceeds the thresholds stated in Section 3.2 from each of the five data sets (Ascension Island L-band and VHF; Huancayo VHF and L-band; Manila VHF), and the second showing the same percentages as calculated from the model. The data used in generating the first pair of plots were limited to times of low geomagnetic activity ($K_p \leq 20$), but no limits were placed on SSN .

The data from Ancon and Kwajalein were too limited in local time to make comparable figures for those two data sets. In comparing Ancon to Huancayo, we found (much to our relief) that when the Huancayo VHF data were limited to the times and conditions covered by the Ancon VHF data, the variations seen in the two data sets were very similar. Thus, we assume that if the model behavior is correct for Huancayo, it is probably quite good for Ancon as well. Kwajalein, however, is another story.

Figure 23 shows the model results for near-overhead geometry at Kwajalein. (The two vertical dotted lines indicate the GMT range covered by the Kwajalein data set.) This behavior is somewhat similar to Manila, but with more scintillation activity in the local

Ascension Is.-MARISAT (L-band)

Percent of Time $S_4 > 0.5$



Percent of Time $S_4 > 0.8$

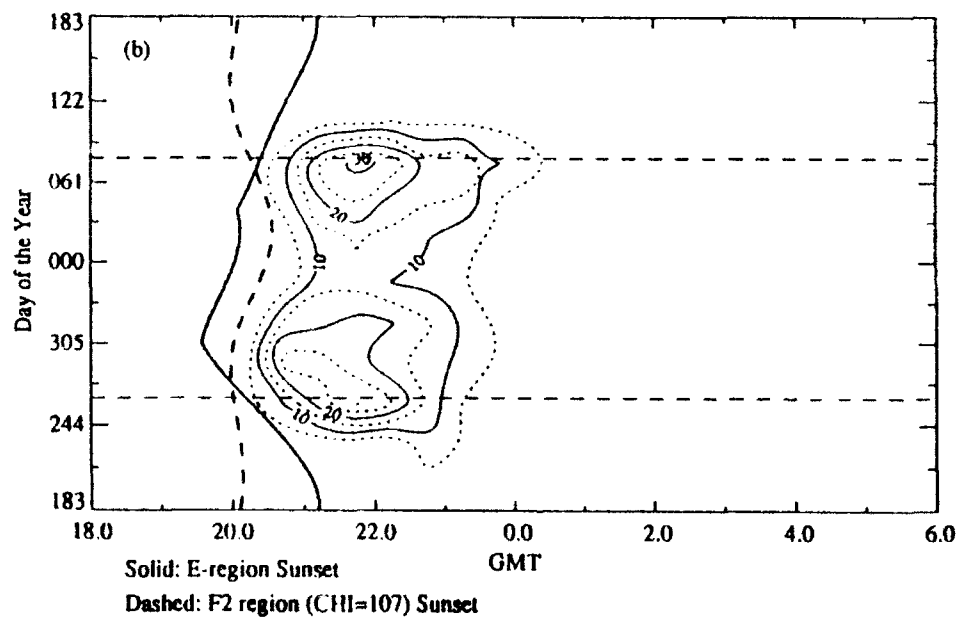
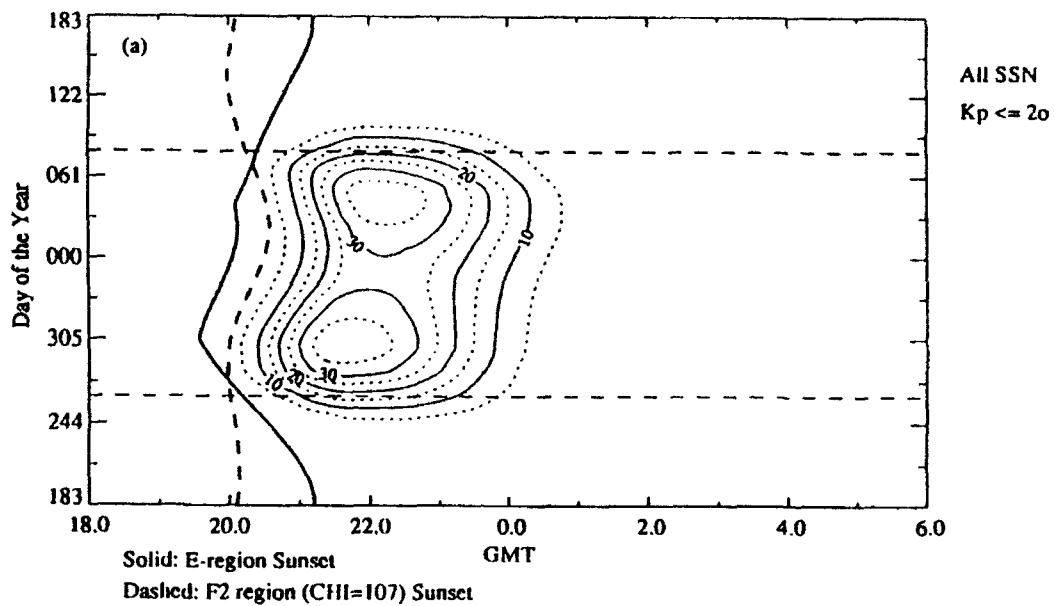


Figure 13: (a) Contours of the percent of observations with $S_4 > 0.5$ as a function of GMT and day of the year from the Ascension Island (L-band) data set, $K_p \leq 20$. (b) Same as in (a) for $S_4 > 0.8$. Heavy solid curve is the time of E-region sunset, heavy dashed curve is the time of F-region sunset ($\chi = 107^\circ$), and the two dashed horizontal lines indicate the two equinoxes.

Ascension Is.-MARISAT (L-band) [MODEL]

Percent of Time $S_4 > 0.5$



Percent of Time $S_4 > 0.8$

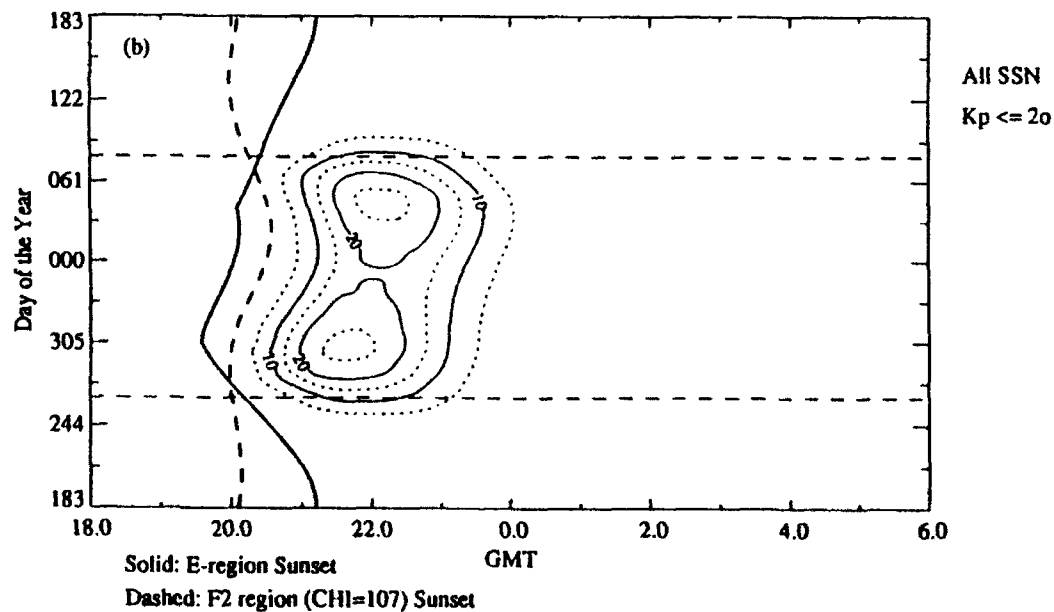


Figure 14: (a) Model results for Ascension Island (L-band) corresponding to the data shown in 13(a). (b) Model results for Ascension Island (L-band) corresponding to the data shown in 13(b).

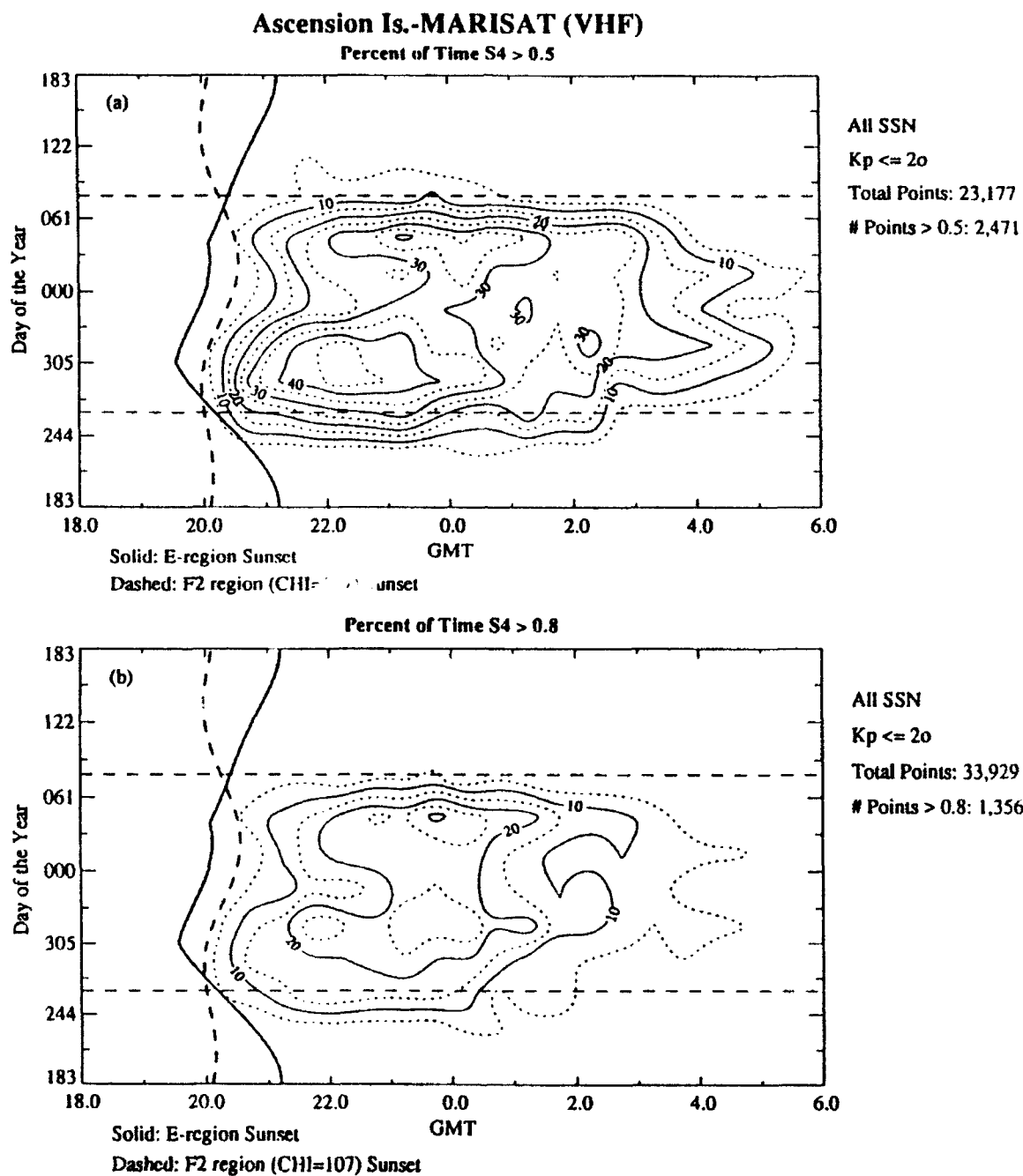


Figure 15: (a) Contours of the percent of observations with $S_4 > 0.5$ as a function of GMT and day of the year from the Ascension Island (VHF) data set, $K_p \leq 20$. (b) Same as in (a) for $S_4 > 0.8$. Heavy solid curve is the time of E-region sunset, heavy dashed curve is the time of F-region sunset ($\chi = 107^\circ$), and the two dashed horizontal lines indicate the two equinoxes.

Ascension Is.-MARISAT (VHF) [MODEL]

Percent of Time $S_4 > 0.5$

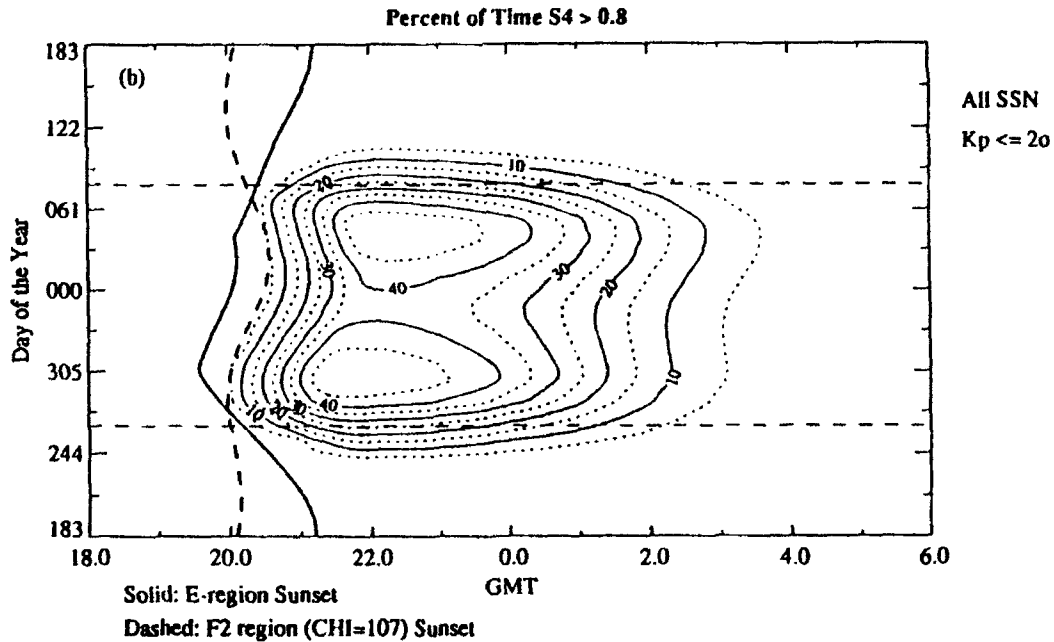
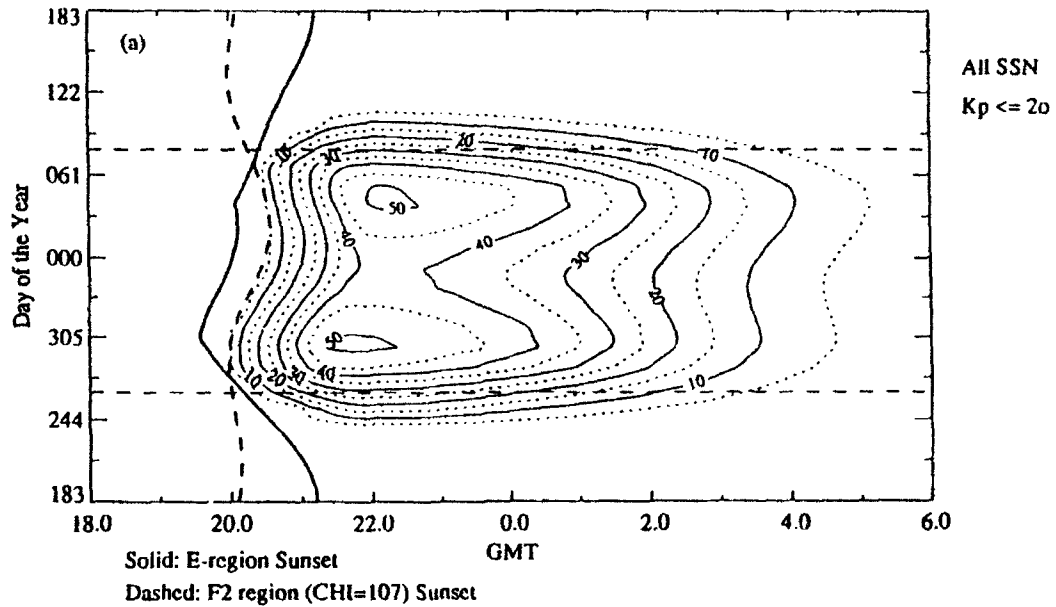
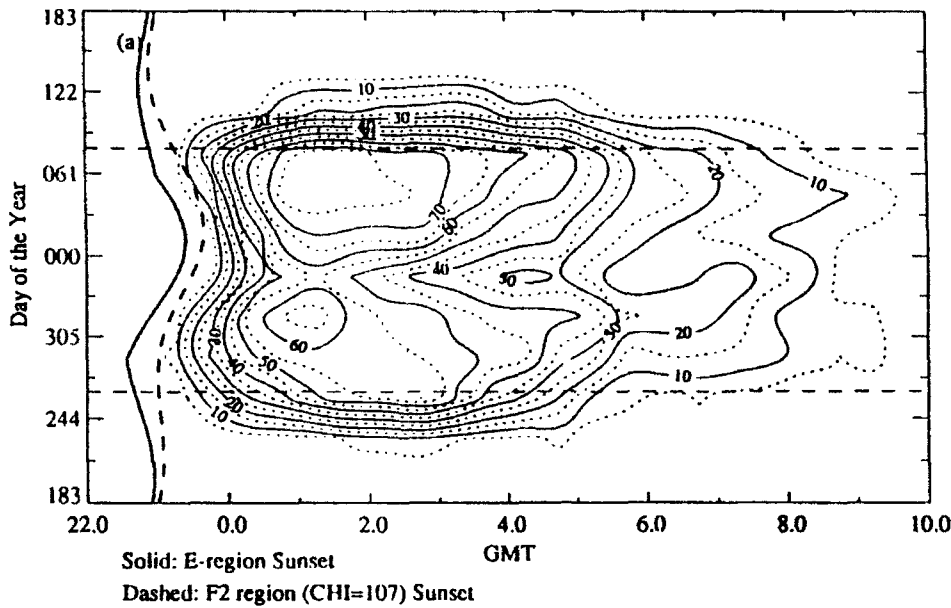


Figure 16: (a) Model results for Ascension Island (VHF) corresponding to the data shown in 15(a). (b) Model results for Ascension Island (VHF) corresponding to the data shown in 15(b).

Huancayo-MARISAT (VHF)

Percent of Time $S_4 > 0.5$



Percent of Time $S_4 > 0.8$

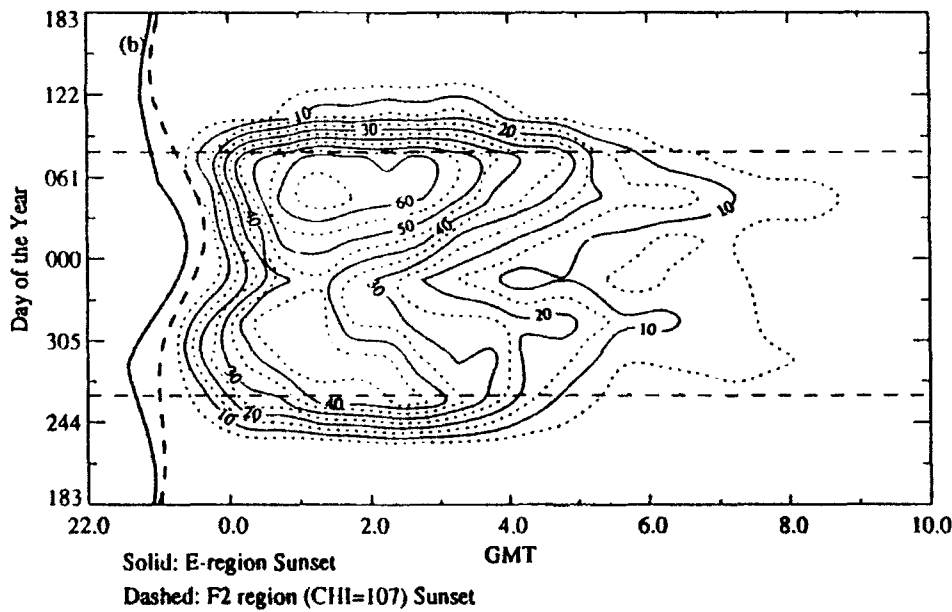


Figure 17: (a) Contours of the percent of observations with $S_4 > 0.5$ as a function of GMT and day of the year from the Huancayo (VHF) data set, $K_p \leq 20$. (b) Same as in (a) for $S_4 > 0.8$. Heavy solid curve is the time of E-region sunset, heavy dashed curve is the time of F-region sunset ($\chi = 107^\circ$), and the two dashed horizontal lines indicate the two equinoxes.

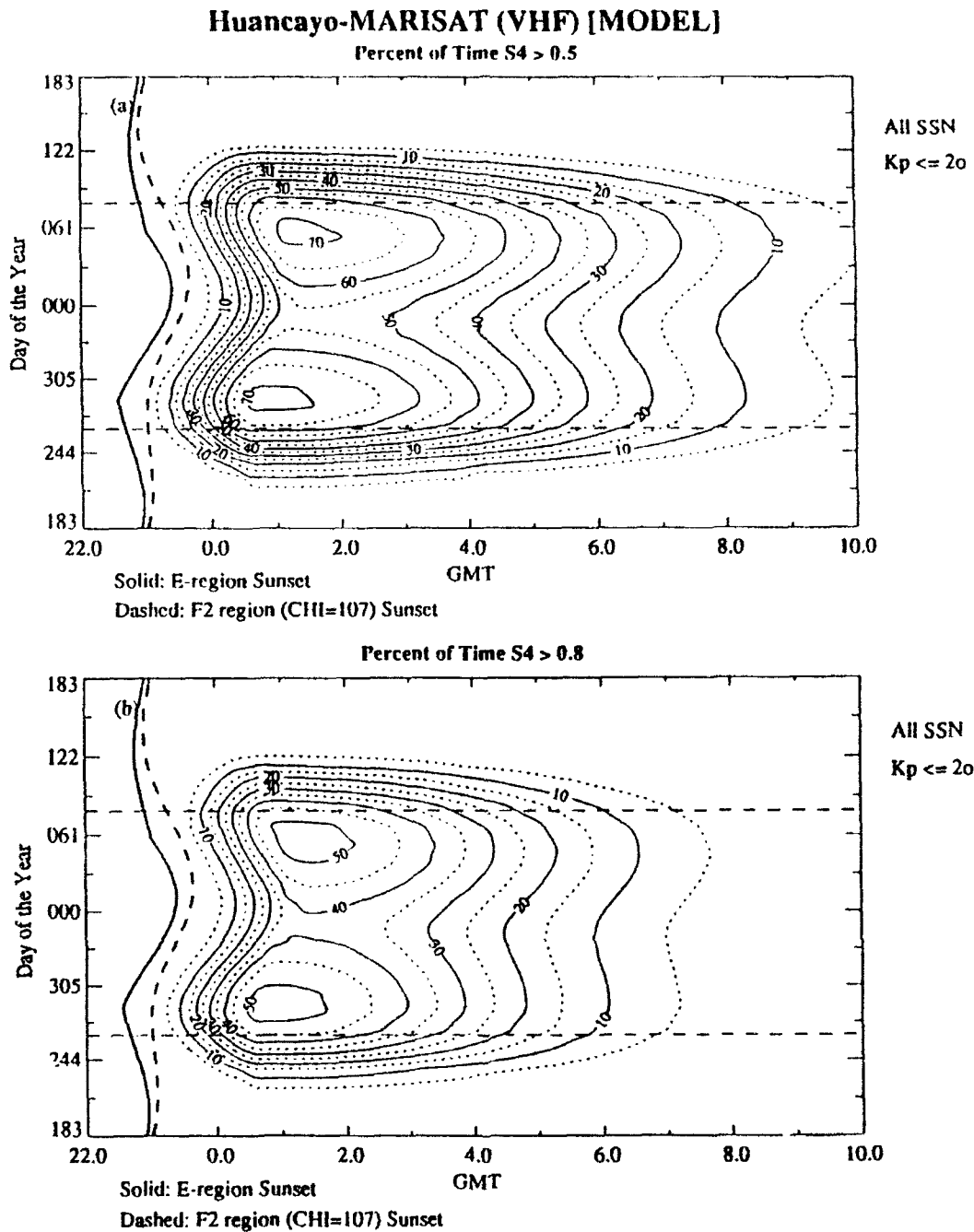


Figure 18: (a) Model results for Huancayo (VHF) corresponding to the data shown in 17(a).
(b) Model results for Huancayo (VHF) corresponding to the data shown in 17(b).

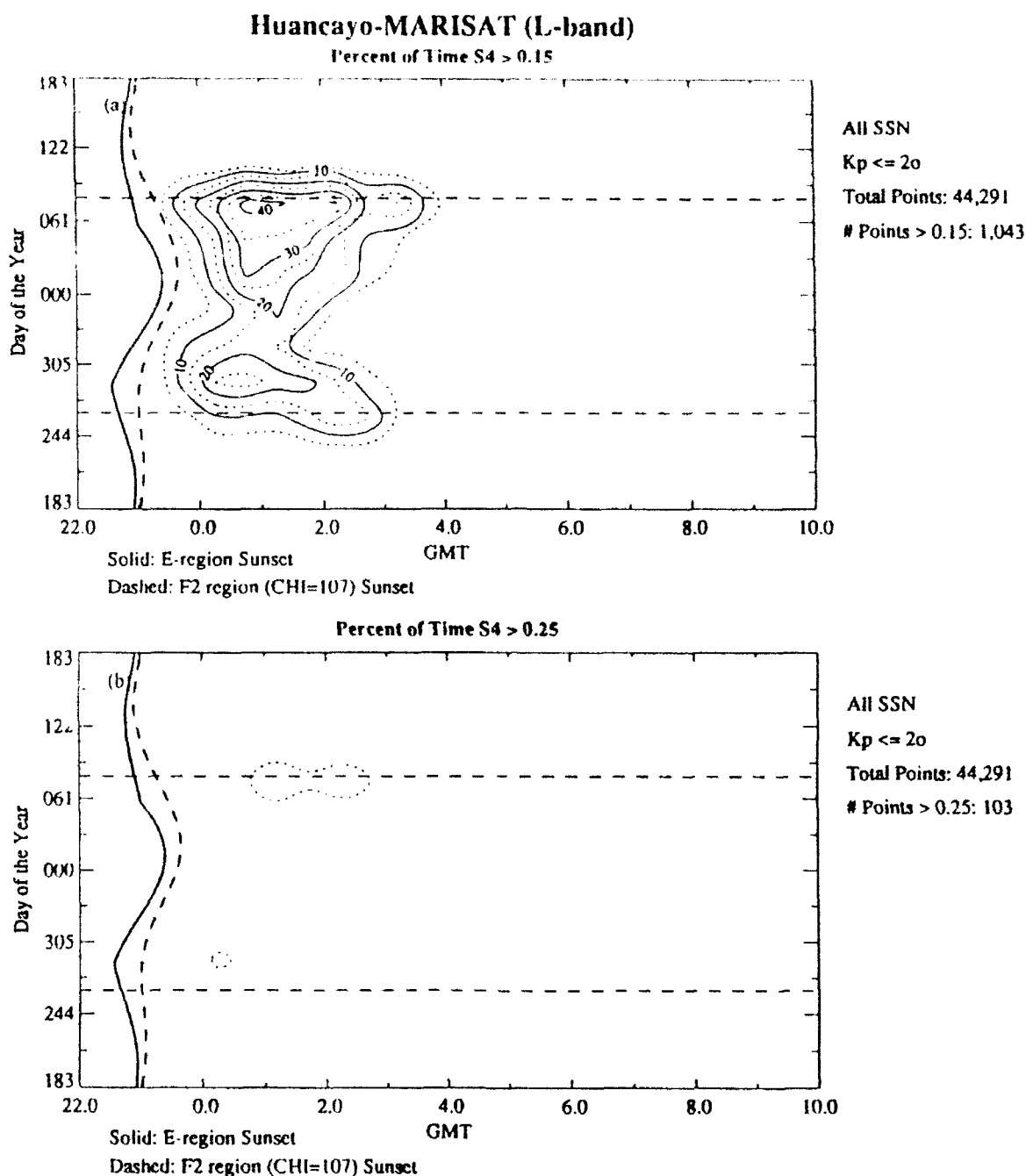


Figure 19: (a) Contours of the percent of observations with $S_4 > 0.5$ as a function of GMT and day of the year from the Huancayo (L-band) data set, $K_p \leq 20$. (b) Same as in (a) for $S_4 > 0.8$. Heavy solid curve is the time of E-region sunset, heavy dashed curve is the time of F-region sunset ($\chi = 107^\circ$), and the two dashed horizontal lines indicate the two equinoxes.

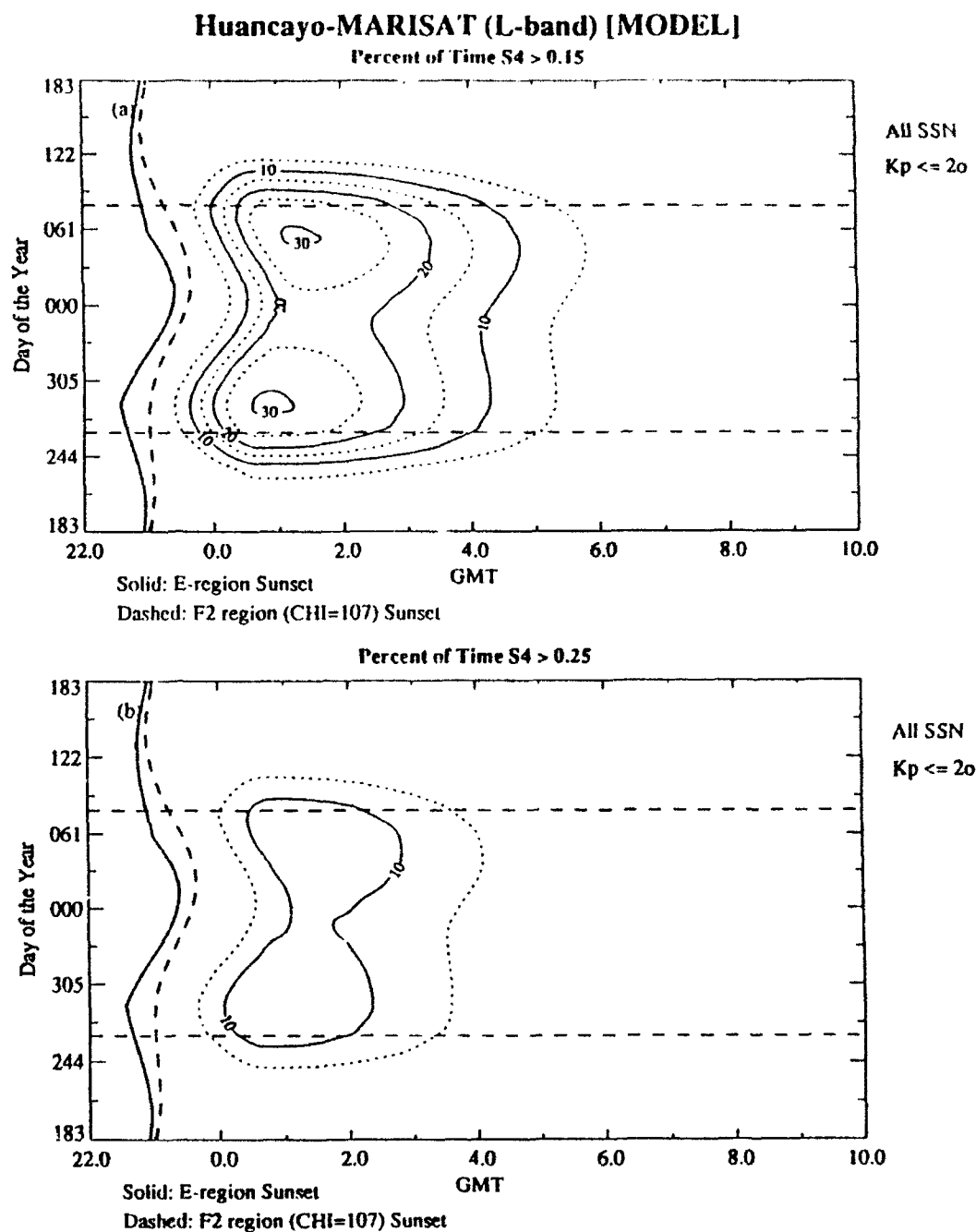
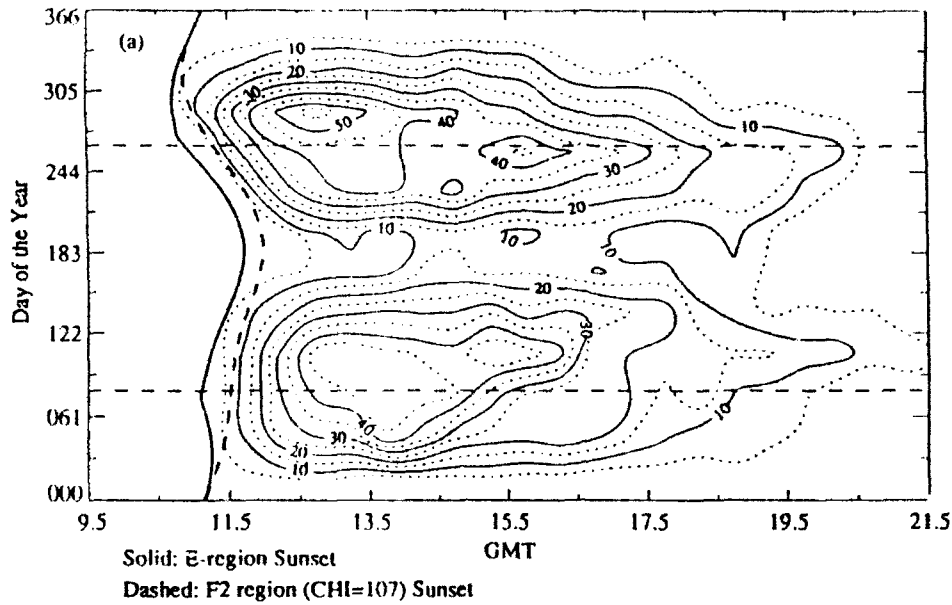


Figure 20: (a) Model results for Huancayo (L-band) corresponding to the data shown in 19(a). (b) Model results for Huancayo (L-band) corresponding to the data shown in 19(b).

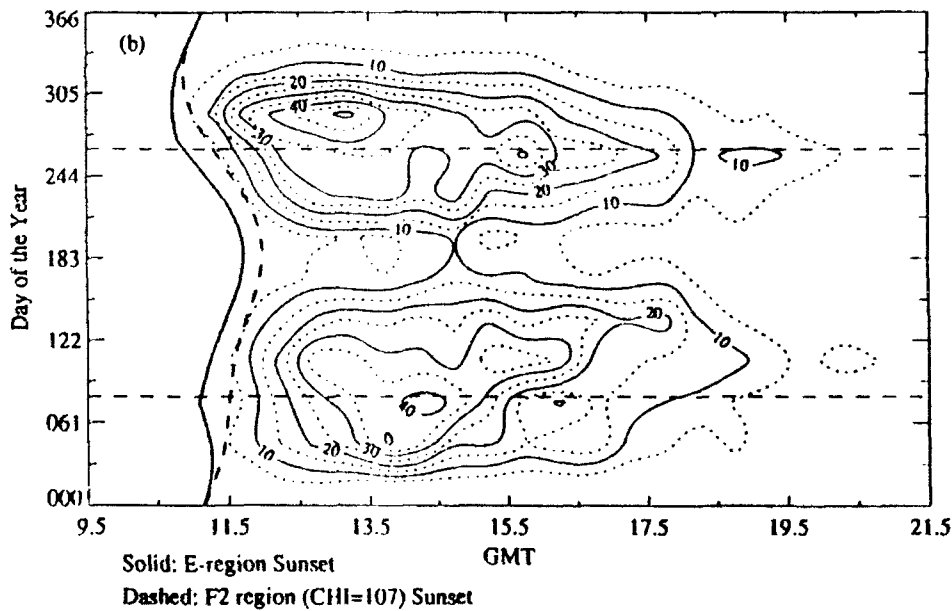
Manila-FLEETSAT (VHF)

Percent of Time $S_4 > 0.5$



All SSN
 $K_p \leq 20$
Total Points: 28,621
Points > 0.5 : 3,335

Percent of Time $S_4 > 0.8$



All SSN
 $K_p \leq 20$
Total Points: 28,621
Points > 0.8 : 2,349

Figure 21: (a) Contours of the percent of observations with $S_4 > 0.5$ as a function of GMT and day of the year from the Manila (VHF) data set, $K_p \leq 20$. (b) Same as in (a) for $S_4 > 0.8$. Heavy solid curve is the time of E-region sunset, heavy dashed curve is the time of F-region sunset ($\chi = 107^\circ$), and the two dashed horizontal lines indicate the two equinoxes.

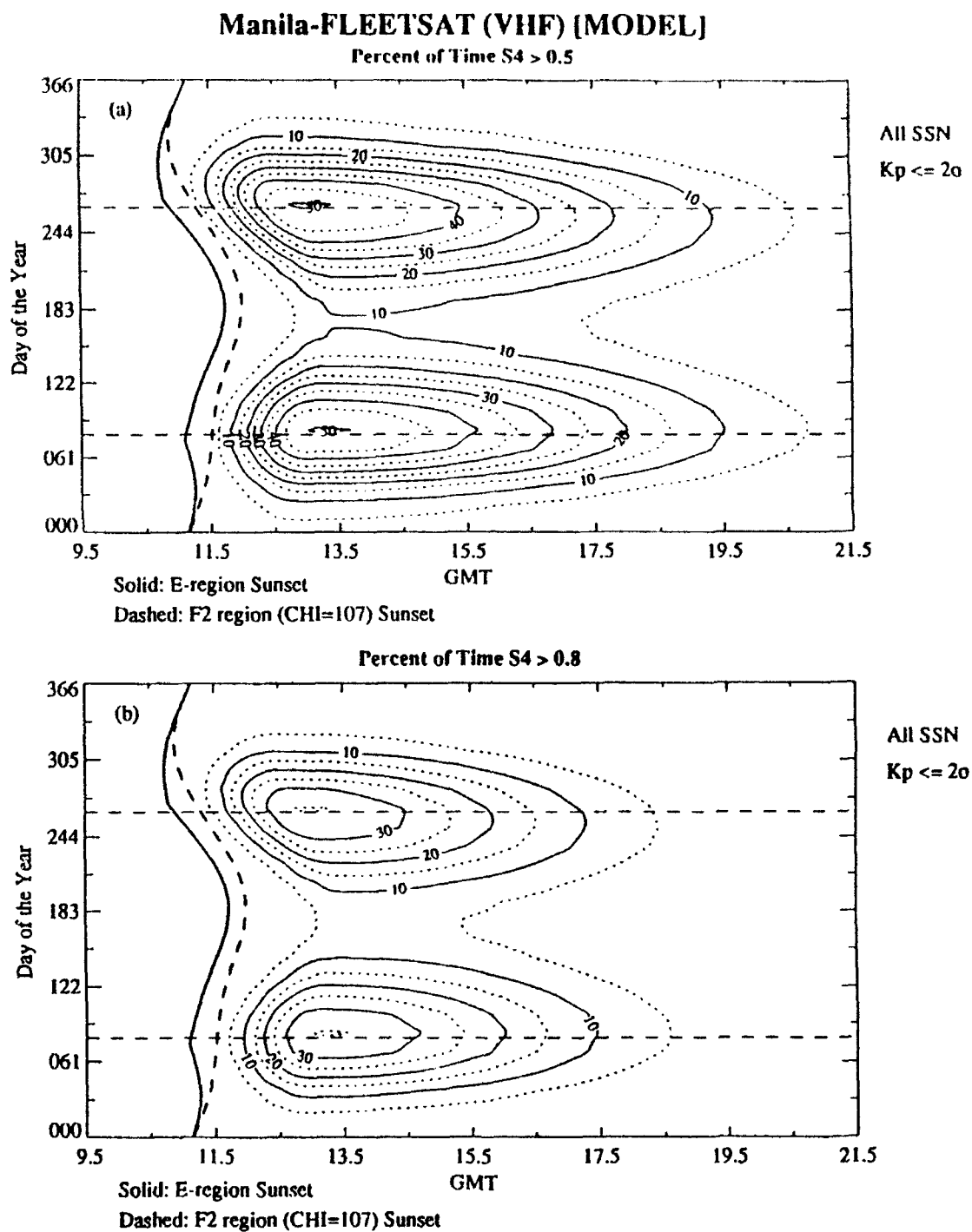
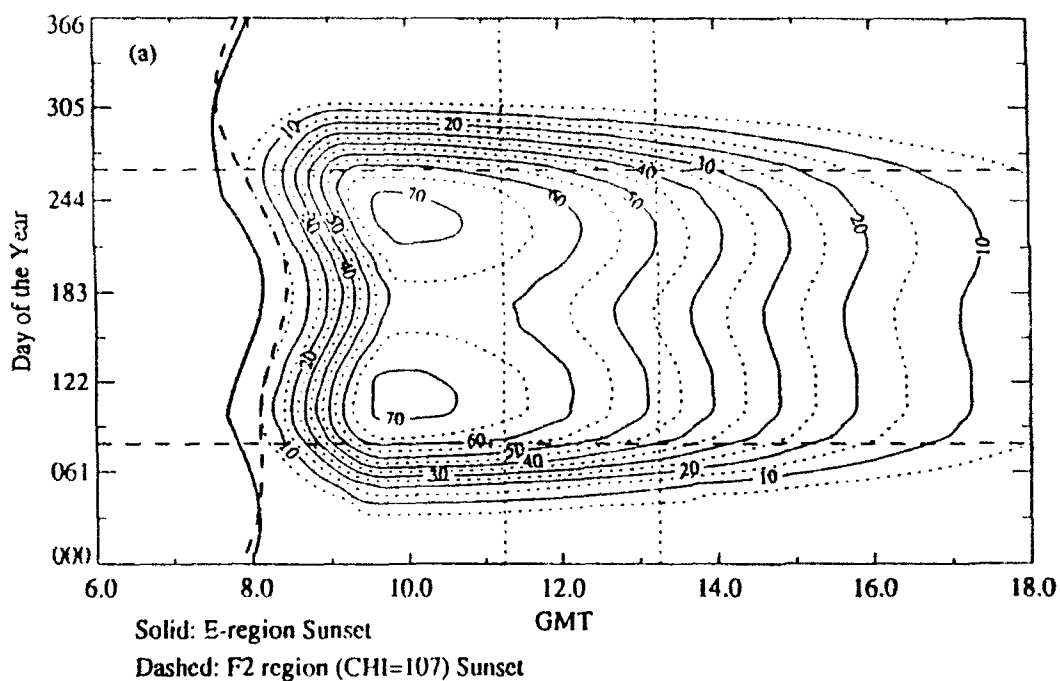


Figure 22: (a) Model results for Manila (VHF) corresponding to the data shown in 21(a).
(b) Model results for Manila (VHF) corresponding to the data shown in 21(b).

Kwajalein - WIDEBAND (VHF) [MODEL]

Percent of Time $S_4 > 0.5$



Percent of Time $S_4 > 0.8$

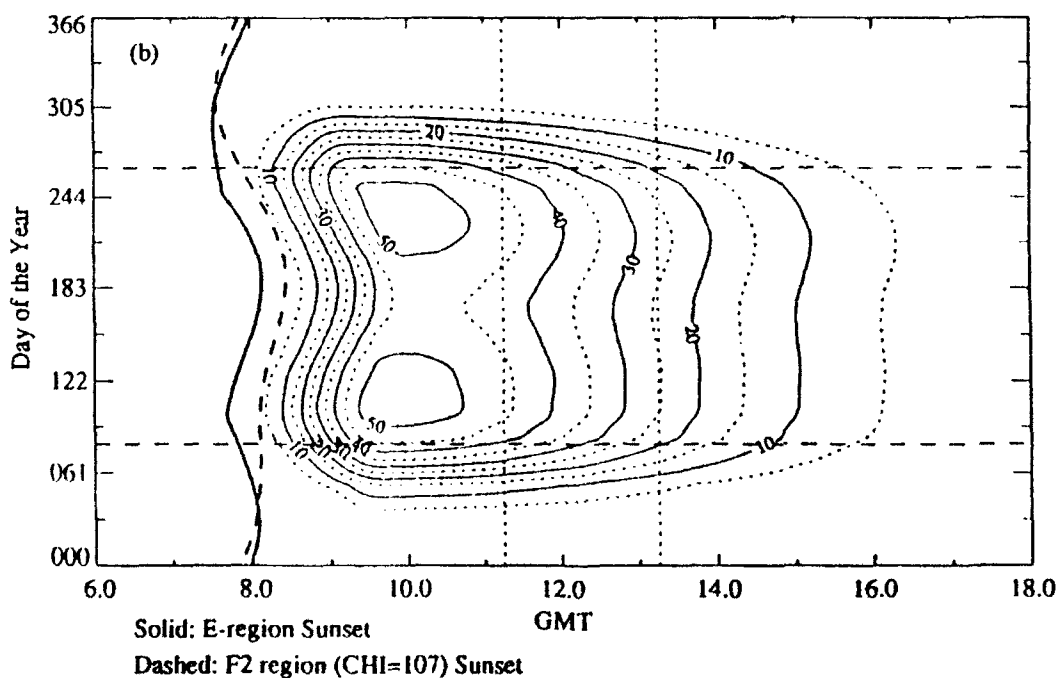


Figure 23: Model results for Kwajalein (near-overhead case). Layout and labeling are as in similar plots in Figures 13-22. The two vertical dotted lines indicate the GMT range covered by the Kwajalein-WIDEBAND (VHF) data set.

summer. Figure 24 shows a comparison of the post-sunset data from Kwajalein with data from Manila limited to the same time-past-sunset interval as the Kwajalein set (roughly 0330 to 0530 t_e). The summer "fill-in" is seen to be far greater at Kwajalein than at Manila, and greater as well than called for in the model. This was also noted as a major difference between Kwajalein and Ancon in previous modeling [Secan, 1989]. We were unable to reconcile this feature at Kwajalein with the observed behaviors at the other stations in the database, although as can be seen in Figure 23 the model does tend to call for a more noticeable "fill" in the summer than at the other stations.

In obtaining the fits as shown in these figures, it was often necessary to degrade the quality of the fit at one station (or season, or time) in order to fit the observed behavior at the other stations (seasons, times). A major problem of this type can be noted in the peak percentages at the two seasonal maxima at the various stations. In each case, one of the maxima is higher than the other. Unfortunately, there is no systematic rule that can be extracted from the data in hand. The higher maximum occurs near the vernal (post-summer) equinox at Huancayo (and Ancon), the autumnal (pre-summer) equinox at Ascension Island, and the autumnal (pre-winter) equinox at Manila. The Kwajalein data show a broad peak throughout the summer. While it would be simple to add a seasonal asymmetry to the occurrence peaks in the model (requiring only a minor alteration to Equation [12]), the lack of a systematic behavior has forced us to exclude this variation and simply produce symmetric peaks with peak occurrence values midway between the observed values.

3.8 Geomagnetic Activity Effects.

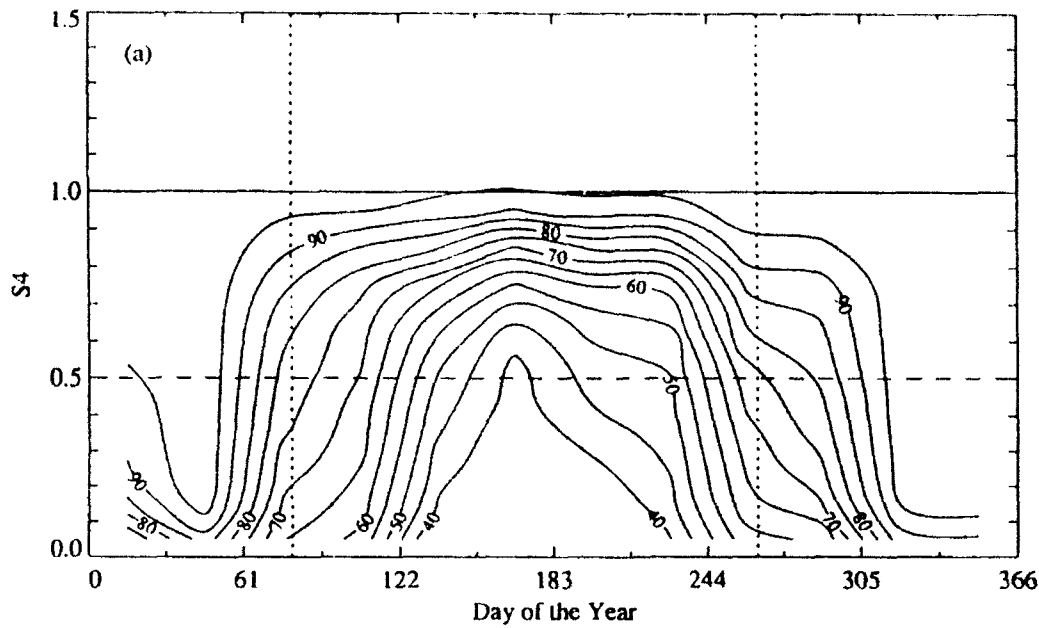
WBMOD has never included effects of geomagnetic activity on scintillation levels in the equatorial region. The reason is that there has been little consensus on what the effects are, aside from indications that increased levels of activity tend to suppress post-sunset scintillation and may enhance post-midnight scintillations. Our plan of attack for investigating the possibility of adding these effects is as follows:

1. Review the existing literature discussing (a) the observational evidence and (b) current theories of the effects of geomagnetic activity on equatorial scintillation.
2. Determine which parameters to use in partitioning the scintillation data and in the final modeling. For example, the minimum D_{st} observed during the previous day, K_p at sunset, $\sum K_p$ over the previous twelve hours, etc. This determination will be based on the results of the literature review.
3. Conduct both statistical and case studies from the equatorial database of the behavior of scintillation as functions of the various geomagnetic parameters.
4. If a systematic behavior is found, develop an empirical model for the effect found.

3.8.1 Literature Review. This section contains the results of a preliminary literature search for prior research work on the subject of geomagnetic control, or influence, on equa-

Kwajalein - WIDEBAND (VHF)

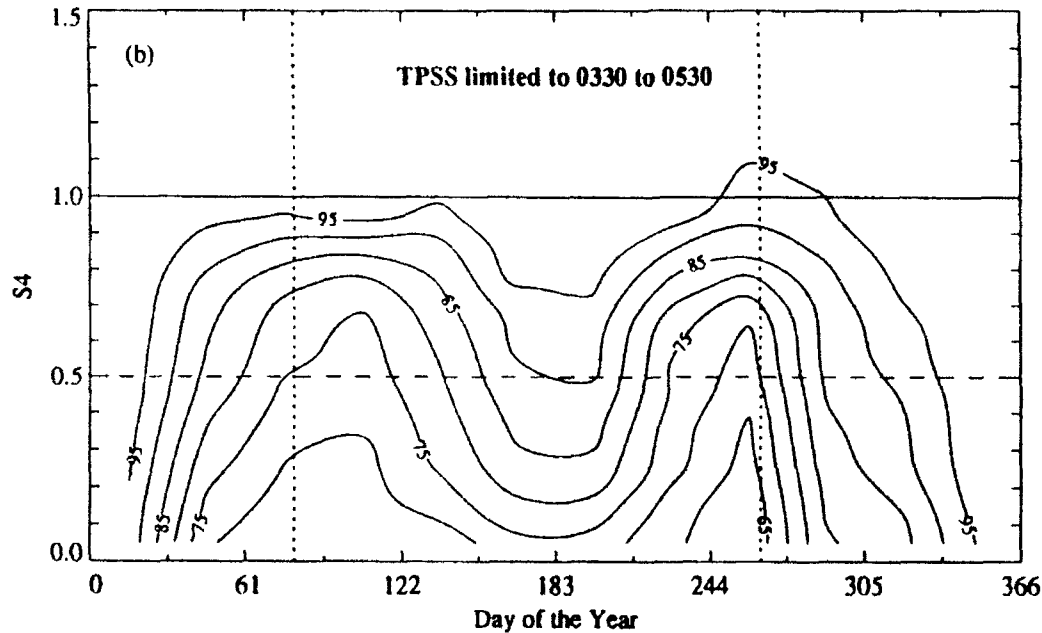
Cumulative Distribution (%)



All SSN
All Kp
Total Points: 10,191

Manila - FLEETSAT (VHF)

Cumulative Distribution (%)



All SSN
All Kp
Total Points: 12,334

Figure 24: Cumulative distribution of S_4 as a function of day of the year (a) from the Kwajalein-WIDEBAND (VHF) data set, (b) from the Manila-FLEETSAT (VHF) data set (limited to the t_e period covered by the Kwajalein data set). The vertical dotted lines indicate the equinoxes.

torial scintillation. It must be noted that the articles cited in this report do not represent a comprehensive list of all publications, but are rather a selection of the voluminous papers on the subject. Since much of the available literature examines geomagnetic effects on Equatorial Spread F (ESF), and the ESF phenomenon is intimately related to equatorial radio scintillation, the literature search will consider geomagnetic control or influence on ESF as well as radio scintillation. There is considerable disagreement on the proper measure of the level of geomagnetic activity, but the two most commonly utilized in the recent literature seem to be K_p and D_{st} , whereas much of the early work used sunspot activity as the measure of geomagnetic activity. As background, some papers demonstrating an understanding of the basic processes producing scintillation will be included, even where direct geomagnetic influence on scintillation is not a topic. Early work on equatorial scintillation often used radio star sources to study scintillation phenomena, [Wright *et al.*, 1956; Koster, 1958; Koster and Wright, 1960]. These works focused on radio scintillation measurements rather than on ESF measurements and revealed the close correlation between ESF and equatorial scintillation, as well as the first indications of a negative correlation between equatorial scintillation and increased geomagnetic activity.

Satellite scintillation work improved the studies, and early work strengthened the suggestion that high geomagnetic activity often has an inhibitory effect on equatorial scintillation. Koster [1972] used the K_p index to show that for lower values of K_p ($\sum K_p < 30$), there is no clear correlation with scintillation; however, for large values of K_p ($\sum K_p > 30$) there is a strong negative correlation with scintillation. Mullen [1973] compared ATS-3 scintillation data (SI) and D_{st} data, and showed evidence that scintillation occurrence in the June solstice increased during periods of magnetic activity, but that the general effect of magnetic activity appears to be a suppression of seasonal scintillation occurrence, with an annual distribution tending toward uniformity.

Present-day work on modeling of equatorial scintillations requires a clear understanding of the basic physical mechanisms at work. Perhaps the onset of this understanding was when strong evidence was presented by Woodman and Laloz [1976] showing that ESF conditions and radio scintillation effects were due to plume-shaped electron density irregularities or bubbles. This study was based on data from the Jicamarca radar data analysis. This understanding of the basic mechanism of radio scintillation began to lead to much better modeling of the details of the mechanisms involved.

Basu and Kelley [1979] reviewed the equatorial scintillation observations and their relationships to the theoretical development of plumes and bubbles, but did not include magnetic activity effects upon scintillation. In addition, Ossakow [1981] reviewed much of the theory and the numerical simulation results for plume structure development, which strongly increased understanding of the basic mechanisms of plume formation due to the Rayleigh-Taylor instability mechanism, though he also did not address the geomagnetic activity influences.

Some early observational work was complicated by the differences between the "range"

and "frequency" types of equatorial spread F. It was shown in *Rastogi* [1980] that the relationship between range spread F and sunspot activity is positive for pre-midnight hours, and strongly negative for post-midnight sectors. The frequency spread F, however, showed relatively little sunspot activity effects.

Aarons et al. [1980] looked at both the seasonal and geomagnetic control of equatorial scintillations in two longitudinal sectors. Although the authors did not delve into the underlying mechanisms, they found that, in general, pre-midnight scintillation is inhibited by magnetic activity (based on K_p) and that during the post-midnight period increased magnetic activity increases scintillation activity under moderate solar flux conditions. A review of the status of ionospheric scintillations was given by *Aarons* [1982]. Although the empirically derived magnetic activity effects upon scintillation were described, the actual mechanisms of control were still undefined. Since the prime driver of the Rayleigh-Taylor mechanism is the ExB drift after sunset forcing the layer to rise and become unstable, it is clear that modeling the geomagnetic effects on scintillations will require an understanding of the equatorial electric fields involved. *Fejer* [1986] presented a summary of the equatorial electric fields associated with magnetic disturbances. He found that the zonal equatorial electric fields often show large and sudden perturbations during geomagnetically disturbed periods, whereas the F-region vertical electric fields do not change significantly with magnetic activity. He also detailed that to first order, perturbation electric fields are westward during the day and eastward at night, and that southward B_z (component of the Interplanetary Magnetic Field) changes seem less effective in disturbing the equatorial electric fields.

Earle and Kelley [1987] have shown that for $K_p > 3$, fluctuations in the magnetospheric electric fields with periods less than about six hours penetrate virtually unattenuated to the equatorial ionosphere, while those with longer periods are shielded out. A clear and concise account of the high latitude effects on the equatorial electrodynamics is given in *Kelley* [1989].

Aarons [1991] introduced a view that the ring current (as determined by the peak excursion of D_{st}) during magnetospheric storms plays a leading role by either directly or indirectly establishing the conditions necessary for equatorial F layer irregularity generation or inhibition. The view that the relationship between the local time and the time of maximum ring-current energy is of primary importance to the development of plumes is emphasized. The theory says that if the maximum ring-current energy (as shown by D_{st}) occurs during the midnight to postmidnight time period, irregularities are generated. If the maximum D_{st} occurs in the early afternoon, then irregularities are inhibited. If, however, the maximum occurs around sunset or shortly after sunset, then there is no effect on the generation of irregularities that night. The behavior of scintillation during a number of individual magnetic storm events were presented to support this view. The weaknesses of this paper are that only individual events were presented, no statistical analysis of a large data set being given, and that the connection between the maximum ring-current energy and the F-layer electric fields is neither clearly presented nor justified by observational data.

Recently a paper by *Kelley and Maruyama* [1992] presented a diagnostic model for equatorial spread F detailing the effect of magnetic activity. This work is based upon the key observation that for short periods (less than six hours), high-latitude electric fields penetrate to low latitudes (see previous section). The basic model used was developed in a previous paper by *Maruyama* [1988]. In this paper, by means of a numerical model, they examined the electric field effects on the generation of ESF in the post-midnight hours.

The above model was designed to run using average zonal electric field patterns published by *Fejer et al.* [1979], based on season and solar-cycle variations. A gaussian-like perturbation was added to simulate an eastward electric field penetration from high latitudes to the average zonal electric field. This perturbation was added in different model runs at different times during the night, and it was found that an increase in the instability growth rate (γ) was not just due to the destabilizing influence of an eastward component of the electric field. The altitude change of the layer and the corresponding decrease in the ion-neutral collision frequency (ν) (which increased the value of the g/ν term) was an important factor. The g/ν term depends on the ratio of the gravitational field to the collision frequency. The model runs showed that, in general, the later in the evening the disturbance occurs, the more effective it is in enhancing instability growth. As would be expected, the perturbation amplitude also plays an important part in determining the growth rate. Thus, the model shows that a reversal of the electric field from zonally westward to zonally eastward, while the main contributor to and initiator of the generation mechanism, does not have absolute and direct control. Indeed, the reversal is sometimes not sufficient by itself to trigger intense ESF. The altitude change of the layer and the corresponding decrease in ion-neutral collision frequency has a large effect in the model, and often is the crucial parameter when determined by the magnitude and duration of the event.

The *Kelley and Maruyama* [1992] study proceeds to examine individual cases, which are quantitatively very well modeled. Electric field data from Jicamarca was used so that comparison to actual plume development could be performed. The caveat was presented that the observational data was limited since the flux tubes involved were so long that no single station could model all necessary parameters. The transequatorial thermospheric wind effects discussed in the *Maruyama* [1988] paper were also not included in the *Kelley and Maruyama* [1992] paper since no observational data existed for the days in question. Although no statistical database was used for analysis, the model does explain the previous observations: that spread F which develops post-midnight does occur more often during periods of magnetic disturbance.

The status of modeling the effect of geomagnetic activity upon equatorial spread F and equatorial radio scintillations is improving. It is clear, however, that there is a tremendous amount of work to be done yet upon this subject, and the time when such models can be used as actual predictors of scintillation is still far away.

3.8.2 Model Development. In developing the way in which WBMOD will reflect the effects of geomagnetic activity on equatorial scintillation, we held to the philosophy

that WBMOD is a climatological (i.e., statistical) rather than a phenomenological model. In other words, the model will attempt to reproduce the behavior seen in the occurrence statistics rather than attempting to model it in terms of a set of "canonical" storm-time behaviors. We have also *not* attempted to include many of the details of the behaviors we have found in the data, in most part because it was almost impossible to find a set of behaviors common to all stations beyond that which we have decided to implement.

In keeping with the modeling philosophy outlined in Section 3.2, we will model the effects of geomagnetic activity on equatorial scintillation in terms of its effect on the probability that plumes will form and grow. This will be done by modifying the η_2 parameter as a function of the level of activity. The modeling effort focused on three issues: (1) what metric should be used to characterize the level of geomagnetic activity (D_{st} , K_p , etc.), (2) what is the effect of changes in this metric in the occurrence statistics, and (3) how can this effect be modeled.

In the work to determine which metric to use, we focused on the following parameters:

1. K_p at the time of the scintillation observation,
2. K_p at sunset ($t_e = 0$, t_e as defined in SR4),
3. D_{st} at the time of the scintillation observation,
4. Minimum D_{st} observed during the previous day and the local time of the minimum.

Although D_{st} is not currently available in either real-time or in forecasts at the USAF Space Forecast Center (a primary customer for the WBMOD upgrade), work is under way to obtain this parameter for use in other space models. The fourth item is an attempt to model the behavior described in *Aarons [1991]* in which the local time that a storm reaches its minimum D_{st} controls the behavior of nighttime scintillation. After some work with these two parameters (the minimum D_{st} and time of the minimum), it became apparent that while they could possibly be useful in a phenomenological model, the changes seen in the occurrence statistics when categorized using these parameters were not that much different (or clearer) than the changes seen in the simpler parameters in the above list. When a successor model to WBMOD that deals with scintillation from a phenomenological standpoint is developed, this set of parameters should be revisited.

Figures 25 through 27 are samples of what we found in this study. These figures show the occurrence statistics of $S_4 > 0.5$ as a function of t_e and day of the year from the Huancayo VHF data set for three ranges of D_{st} (Figure 25), K_p (Figure 26), and K_p at sunset (Figure 27). (The general behavior seen in the Huancayo data is fairly representative of all three stations.) All three figures show the same general behavior as the level of activity increases:

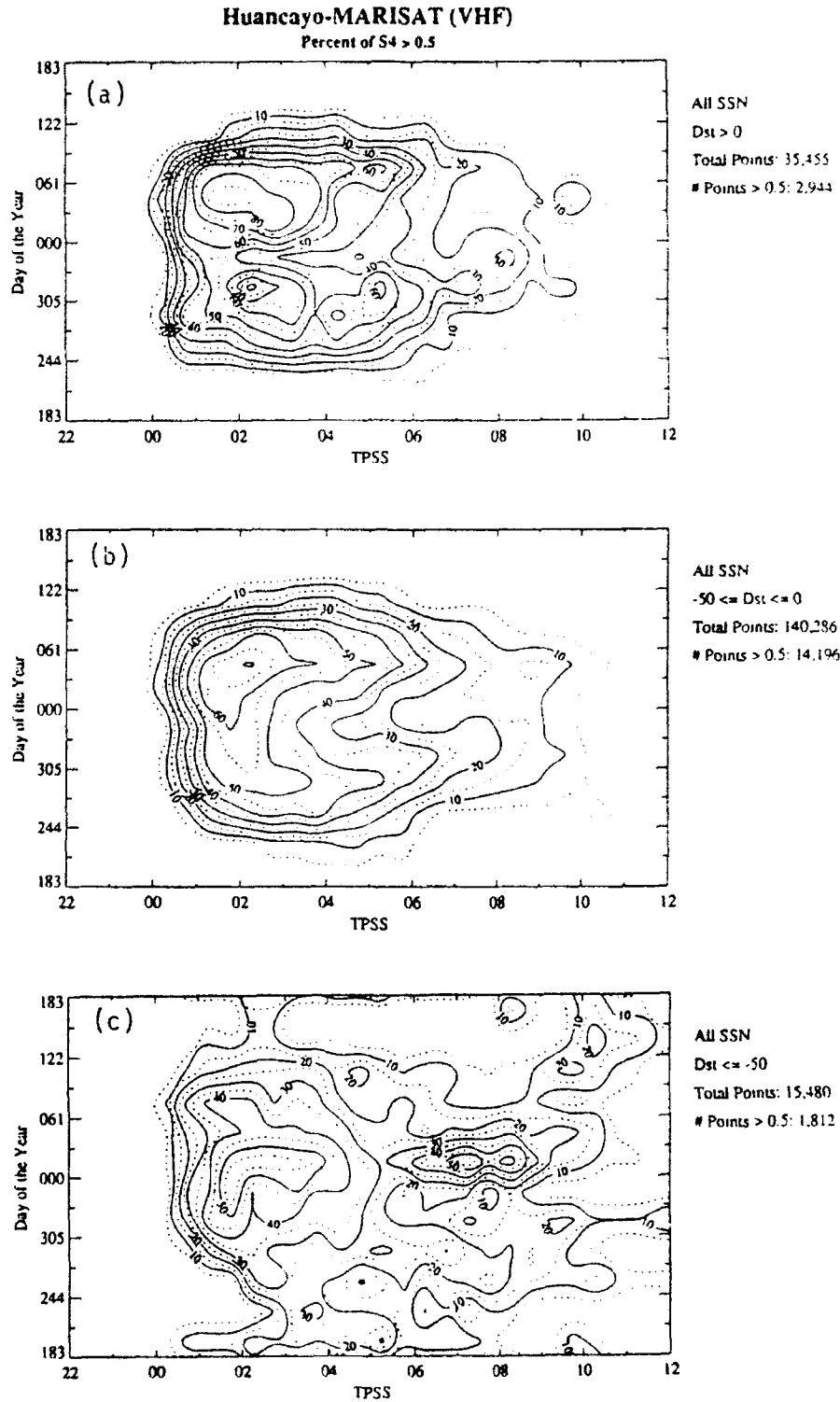


Figure 25: Occurrence statistics of $S_4 > 0.5$ from the Huancayo VHF data set as a function of TPSS (t_e) and day of the year for three levels of geomagnetic activity as measured by D_{st} : (a) $D_{st} > 0$, (b) $0 \geq D_{st} \geq -50$, and (c) $D_{st} < -50$.

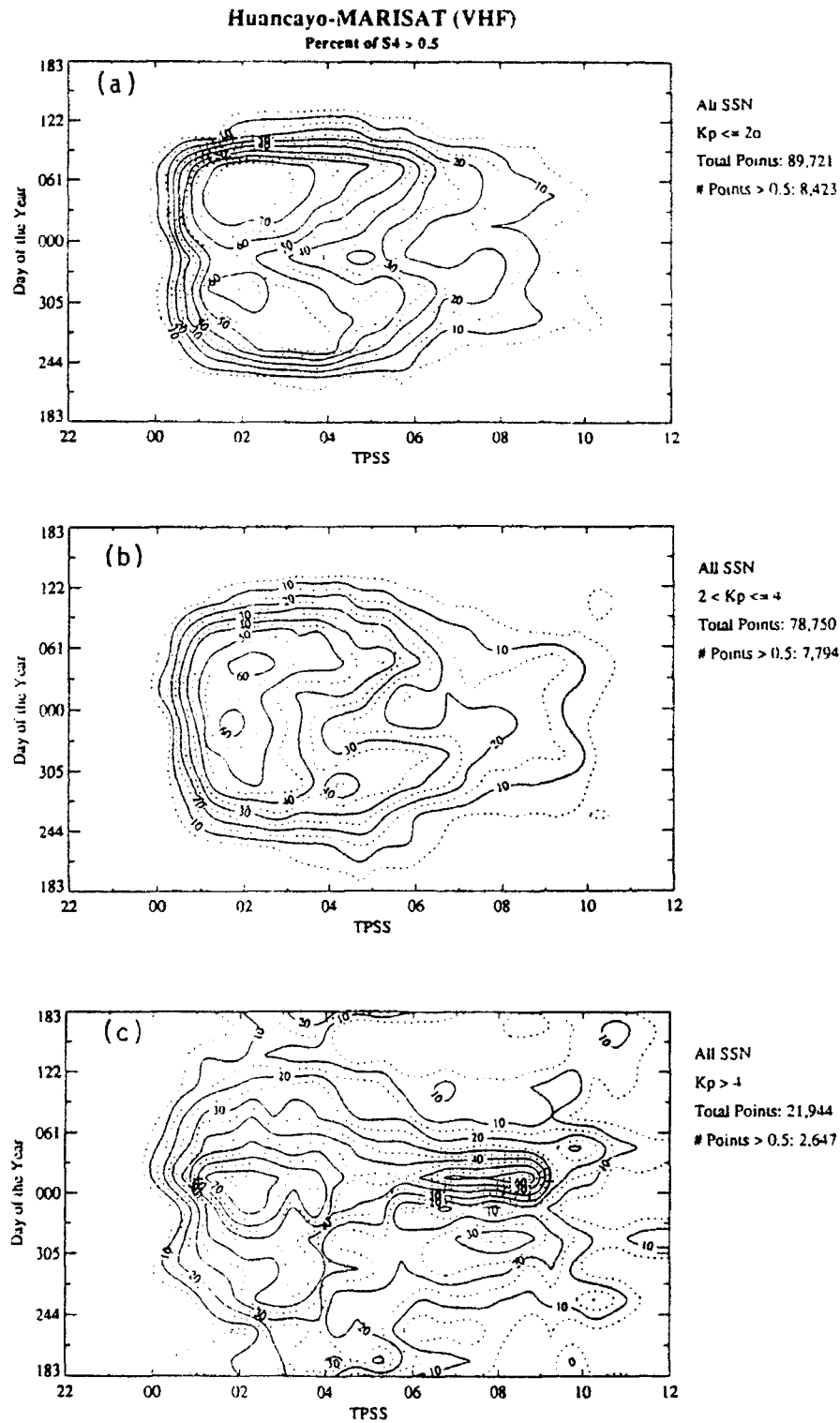


Figure 26: Occurrence statistics of $S_4 > 0.5$ from the Huancayo VHF data set as a function of TPSS (t_e) and day of the year for three levels of geomagnetic activity as measured by K_p : (a) $K_p \leq 2$, (b) $2 < K_p \leq 4$, and (c) $K_p > 4$.

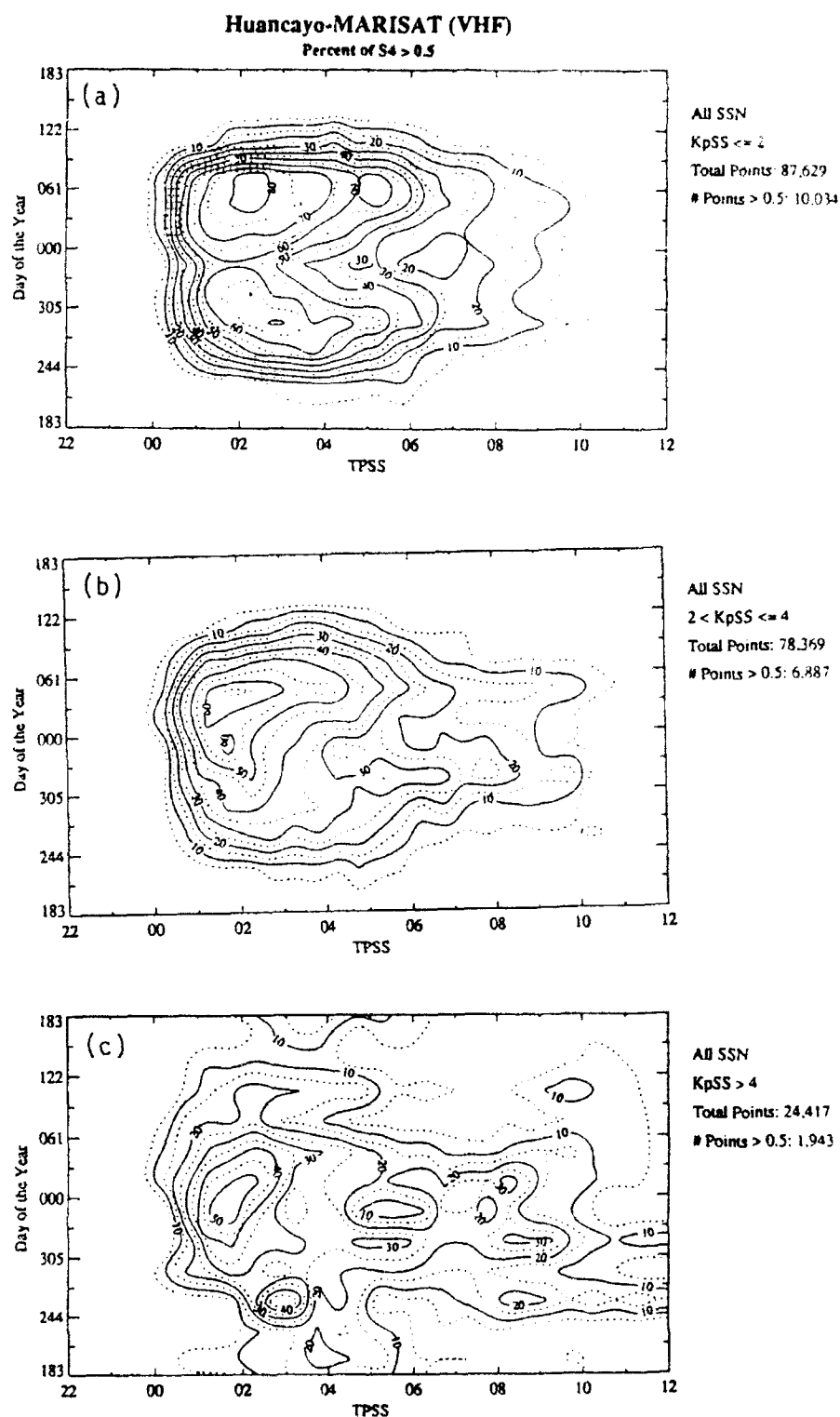


Figure 27: Occurrence statistics of $S_4 > 0.5$ from the Huancayo VHF data set as a function of TPSS (t_e) and day of the year for three levels of geomagnetic activity as measured by K_p at $t_e = 0$: (a) $K_p \leq 2$, (b) $2 < K_p \leq 4$, and (c) $K_p > 4$.

1. The occurrence of scintillation at the post-sunset near-equinoctial peaks decreases (*i.e.*, inhibition of post-sunset plume development).
2. The post-sunset occurrence statistics in the local-summer minimum between the peaks do not change as much, giving rise to the appearance that the two peaks are “merging” into a single peak in local summer.
3. The variation of the occurrence statistics with time become “stretched out” in the sense that the levels become higher in the post-midnight period.

In reviewing these figures, we came to the following conclusions:

1. For a climatological model of scintillation occurrence statistics, the K_p parameter is as good as D_{st} (or, at least, no worse) for characterizing the effects of geomagnetic activity on equatorial scintillation.
2. The post-sunset reduction in the occurrence frequency shows most clearly in the K_p at sunset parameter, and the post-midnight enhancement in the occurrence-frequency levels shows more clearly in the K_p valid at the time of the observation.

These observations will form the basis for the model variation of the $\log(C_k L)$ PDF with geomagnetic activity.

A final note — improvements to this aspect of the model await a better understanding of the exact details of the coupling between processes at work in the magnetosphere and at high latitudes during geomagnetic storms and the observed behavior of scintillation in the equatorial region. Recent papers by *Aarons* [1991] and *Kelly and Maruyama* [1992] are definite steps towards a better understanding, but further work is needed.

4. Propagation Model Development

The propagation model in WBMOD has a known deficiency in the way in which S_4 is calculated for a two-way path. The present work is focused on calculating the expected correlation between scintillation imposed on a signal on the up- and down-links of a two-way path. The basic equation relating S_4 calculated on a one-way path (denoted S_m) and that for the two-way path is

$$S_4^2 = \left(\frac{S_m^2 + 1}{\rho S_m^2 + 1} \right)^2 \left[1 + \rho S_m^2 \left(4 + 2 \frac{\rho S_m^2}{S_m^2 + 1} \right) \right] - 1 \quad (13)$$

where ρ is the correlation between the up- and down-links [*Fremouw and Ishimaru*, 1992]. In the initial implementation of this calculation, we plan to implement Equation [13] with

a user-supplied value for ρ ranging from 0 (full decorrelation) to 1 (full correlation). The guidance provided to the user will be to enter 1 for full correlation (which will be true in most cases) unless there is good reason to enter some value less than 1. When the theory for calculating ρ from the system geometry and the effective scan velocity (V_{eff}) is completed, that theory will be implemented in an upgrade to WBMOD and the user-input value for ρ will serve as an optional user-specified override to the value calculated internally.

5. Conclusion

The next stage in the upgrade of the equatorial model will be completion of modeling the variation of scintillation with geomagnetic activity and inclusion of the variation with the solar cycle (i.e., with *SSN*). When the modeling is completed, the new model will be merged into WBMOD, and the user interface (inputs and outputs) will be modified as necessary for the new model requirements and capabilities.

Once the equatorial modeling is completed, the effort will move to the high latitude region using data from the Wideband, HiLat, and Polar BEAR data sets.

REFERENCES.

- Aarons, J., Global morphology of ionospheric scintillations, *Proc. IEEE*, 70, 360, 1982.
- Aarons, J., The role of the ring current in the generation or inhibition of equatorial F layer irregularities during magnetic storms, *Radio Sci.*, 26, 1131, 1991.
- Aarons, J., J. P. Mullen, J. P. Koster, R. F. da Silva, J. R. Medeiros, R. T. Medeiros, A. Bushby, J. Pantoja, J. Lanat, and M. R. Paulson, Seasonal and geomagnetic control of equatorial scintillations in two longitudinal sectors, *J. Atmos. Terr. Phys.*, 42, 861, 1980.
- Basu, S., S. Basu, and B. K. Kahn, Model of equatorial scintillations from in-situ measurements, *Radio Sci.*, 11, 821-832, 1976.
- Basu, Su. and M. C. Kelley, A review of recent observations of equatorial scintillations and their relationship to current theories of F region irregularity generation, *Radio Sci.*, 14, 471-485, 1979.
- Earle, G. D., and M. C. Kelley, Spectral studies of the sources of ionospheric electric fields, *J. Geophys. Res.*, 92, 213, 1987.
- Fejer, B. G., Equatorial ionospheric electric fields associated with magnetospheric disturbances, in *Solar Wind-Magnetospheric Coupling*, edited by Y. Kamide and J. A. Slavin, p. 519, Terra Scientific, Tokyo, 1986.
- Fejer, B. G., D. T. Farley, R. F. Woodman, and C. Calderon, Dependence of equatorial F region vertical drifts on season and solar cycle, *J. Geophys. Res.*, 84, 5792, 1979.

- Fremouw, E. J. and A. Ishimaru, Intensity scintillation index and mean apparent radar cross section on monostatic and bistatic paths, *Radio Sci.*, **27**, 539-543, 1992.
- Fremouw, E. J. and R. E. Robins, An Equatorial Scintillation Model. *DNA Tech. Rep. DNA-TR-85-333*, Defense Nuclear Agency, Washington, DC, 1985.
- Kelley, M. C., *The Earth's Ionosphere, Plasma Physics and Electrodynamics*, Academic Press, 92-104, 1989.
- Kelley, M. C. and T. Maryuama, A diagnostic model for equatorial spread F, 2. The effect of magnetic activity, *J. Geophys. Res.*, **97**, 1271, 1992.
- Koster, J. R., Radio star scintillations at an equatorial station, *J. Atmos. Terr. Phys.*, **12**, 100, 1958.
- Koster, J. R., Equatorial scintillation, *Planet. Space Sci.*, **20**, 1999, 1972.
- Koster, J. R., and R. W. Wright, Scintillation, spread F, and transequatorial scatter, *J. Geophys. Res.*, **65**, 2303, 1960.
- Maruyama, T., A diagnostic model for equatorial spread F, 1. Model description and application to electric field and neutral wind effects, *J. Geophys. Res.*, **93**, 14,611, 1988.
- Maruyama, T and N. Matuura, Longitude variability of annual changes in activity of equatorial spread F and plasma bubbles, *J. Geophys. Res.*, **89**, 10,903-10,912, 1984.
- Mendillo, M., J. Baumgardner, X. Pi, P. J. Sultan, and R. Tsunoda, Onset conditions for equatorial spread F, *J. Geophys. Res.*, **97**, 13,865, 1992.
- Mullen, J. P., Sensitivity of equatorial scintillation to magnetic activity, *J. Atmos. Terr. Phys.*, **35**, 1187, 1973.
- Ossakow, S. L., Spread-F theories — a review, *J. Atmos. Terr. Phys.*, **43**, 437, 1981.
- Rastogi, R. G., Seasonal and solar cycle variations of equatorial spread-F in the American zone, *J. Atmos. Terr. Phys.*, **42**, 593, 1980.
- Robins, R. E., J. A. Secan, and E. J. Fremouw, A Mid-Latitude Scintillation Model, *DNA-TR-86-381*, Defense Nuclear Agency, Washington, DC, 1986.
- Secan, J. A., Development of Advanced Ionospheric Models in Support of Space-Based Radar Design Studies, Phase II, *NWRA-CR-88-R037*, Northwest Research Associates, Inc., Bellevue, WA, 1989.
- Secan, J. A., WBMOD Model Validation Study, Scintillation Data Catalog, Vol. 1. Equatorial Data Sets, *NWRA-CR-91-R069*, Northwest Research Associates, Inc., Bellevue, WA, 1991.

- Secan, J. A. and E. J. Fremouw, Development of Advanced Ionospheric Models in Support of Space-Based Radar Design Studies, Phase I, *NWRA-CR-88-R022*, Northwest Research Associates, Inc., Bellevue, WA, 1988.
- Tsunoda, R. T., Control of the seasonal and longitudinal occurrence of equatorial scintillations by the longitudinal gradient in integrated E region Pedersen conductivity, *J. Geophys. Res.*, *90*, 447-456, 1985.
- Whitney, H. E., Notes on the Relationship of Scintillation Index to Probability Distributions and Their Uses for System Design, *AFCRL-TR-74-0004*, AD778092, Air Force Cambridge Research Laboratory (now Phillips Laboratory), Hanscom AFB, MA, 1974.
- Woodman, R. F., and C. LaHoz, Radar observations of F region equatorial irregularities, *J. Geophys. Res.*, *81*, 5447, 1976.
- Wright, R. W., J. R. Koster, and N. J. Skinner, Spread F layer echoes and radio star scintillation, *J. Atmos. Terr. Phys.*, *8*, 240, 1956.